https://doi.org/10.5194/egusphere-2026-3827
Preprint. Discussion started: 21 July 2026

Aerosol loading delays droplet activation and suppresses drizzle mode Ka-band radar signatures in LES–LCM simulations of shallow cumulus clouds

Junghwa Lee[1,2], Patric Seifert[1], Tempei Hashino[3], and Yign Noh[4]

[1]Leibniz Institute for Tropospheric Research (TROPOS), Leipzig, Germany
[2]High-Performance Computing Center Stuttgart (HLRS), University of Stuttgart, Stuttgart, Germany
[3]Kochi University of Technology, Kami, Japan
[4]Yonsei University, Seoul, Republic of Korea

Correspondence: Junghwa Lee (junghwa.lee@tropos.de)

Abstract. This article investigates how variations in aerosol loading affect droplet activation and the production of warm rain in shallow cumulus clouds. It is also examined whether the resulting differences can be identified and quantified using $35\,\mathrm{GHz}$ Ka-band radar signatures and how these relationships depend on the cloud life-cycle stage. Three idealized large-eddy simulations, T13 (clean, aerosol number concentration $N_\mathrm{a} = 100\,\mathrm{cm}^{-3}$), T53 (intermediate, $N_\mathrm{a} = 1000\,\mathrm{cm}^{-3}$), and T73 (polluted, $N_\mathrm{a} = 5000\,\mathrm{cm}^{-3}$), coupled to a Lagrangian cloud model (LES–LCM), are conducted with a fixed aerosol size-distribution shape under identical thermodynamic conditions based on the Barbados Oceanographic and Meteorological Experiment (BOMEX). Persistent particle tracking is used to reconstruct Lagrangian histories of super-droplets. Analysis of droplet activation and growth statistics shows that clusters of relative humidity (RH) values distinguish core-like and entrained-shell-like activation pathways. The simulation results further show that increased aerosol loading reduces the temporal window available for droplet activation, spectral broadening, and collision–coalescence. Accordingly, approximately 20.1 %, 15.3 %, and 15.0 % of trajectories reach drizzle size ($r \geq 40\,\mathrm{\mu m}$) in the clean, intermediate, and polluted cases, respectively. Mixing diagnostics shift toward more deactivation-dominated behavior with increasing aerosol loading. These findings suggest that aerosol-dependent microphysical pathways remain detectable in Ka-band Doppler radar signatures. Therefore, Ka-band radar observations provide an observationally testable signature of delayed activation and suppressed warm-rain production, while it shall be noted that knowledge about the evolution state of the cloud system is essential for drawing conclusions about aerosol effects.

1 Introduction

Clouds of shallow cumulus over the ocean in the subtropics, or trade wind clouds, are an important testing ground for understanding the climate system. Due to their high frequency of occurrence, these clouds significantly affect the amount of moisture and energy in the lower troposphere, while also providing a significant source of shortwave albedo and cloud feedback in climate models (Siebesma et al., 2003; van Zanten et al., 2011; Bony et al., 2017). The process of producing warm rain in these clouds occurs at or near the transition between precipitating and non-precipitating conditions (Grabowski and Wang,

https://doi.org/10.5194/egusphere-2026-3827
Preprint. Discussion started: 21 July 2026

2009; Stevens and Feingold, 2009; Hoffmann et al., 2017), and small changes in cloud condensation nuclei (CCN) may shift the outcome well beyond what the perturbation alone would suggest. Shallow cumulus clouds are therefore well suited for following how aerosol loading modifies the path from activation to collector-drop formation.

Aerosol–cloud interactions constitute one of the most significant sources of uncertainty in anthropogenic radiative forcing estimates and predictive models for regional precipitation variability (Boucher et al., 2013; Bellouin et al., 2020; Forster et al., 2021). Most of this uncertainty traces back to warm clouds, where even slight changes in CCN can significantly alter the droplet size distribution, resulting in more numerous but smaller cloud droplets, which suppress collision–coalescence and delay drizzle formation (Twomey, 1977; Albrecht, 1989; Pruppacher and Klett, 1997; Stevens and Feingold, 2009). Quantifying these dependencies in specific cloud regimes has nonetheless proved remarkably difficult.

Higher concentrations of CCN cause lower peak supersaturation and delay activation because the condensational sink is related to the number of droplets present in the air (Twomey, 1959; Pruppacher and Klett, 1997; Grabowski and Wang, 2013; Pinsky et al., 2013). This leads to an increase in competition for water vapor and therefore narrows the early size spectrum prior to the development of a precipitation-mode tail (Khain et al., 2004; Grabowski and Wang, 2009; Stevens and Feingold, 2009). Observations have associated higher aerosol levels with both smaller droplets and weaker drizzle signatures in warm clouds (Feingold et al., 2003; Rosenfeld et al., 2014; Fan et al., 2020). Whether activated droplets go on to produce warm rain depends on how quickly the droplet size distribution expands beyond what can be achieved through diffusional growth alone. The time required for the formation of collector droplets varies based on droplet number concentration, turbulence level, and prior condensational growth history (Pruppacher and Klett, 1997; Grabowski and Wang, 2009, 2013; Grabowski and Abade, 2017). With an increase in aerosol concentration, the transition to the collector-drop stage is further delayed due to decreased collision efficiency in high-droplet-concentration environments (Albrecht, 1989; Khain et al., 2004; Stevens and Feingold, 2009). The extent of this effect is not constant and is strongly influenced by the role entrainment and mixing play in reshaping the droplet distribution through evaporation in core and shell regions of the cloud (Baker et al., 1980; Burnet and Brenguier, 2007; Lehmann et al., 2009; Hoffmann et al., 2015; Hoffmann and Feingold, 2019). It remains uncertain how an increase in aerosol concentration alters the relative contribution of these pathways and how it ultimately affects the timing of rain initiation.

Droplet activation depends on the principles of Köhler theory, the size and composition of dry aerosols, and the supersaturation a given droplet will experience (Köhler, 1936; Pruppacher and Klett, 1997; Petters and Kreidenweis, 2007). Within an ascending air mass, supersaturation occurs as the result of a competition between the production of supersaturation from adiabatic cooling and the reduction of supersaturation due to droplet growth (Twomey, 1977; Seinfeld and Pandis, 2016). Within a turbulent cloud, however, the competition for supersaturation is not uniform across different locations. Different updraft velocities, varying rates of entrainment, and heterogeneous mixing expose air parcels to distinctly different histories of supersaturation. Droplet activation has therefore been shown to differ greatly in both time and space (Shaw, 2003; Lanotte et al., 2009; Devenish et al., 2012; Grabowski and Wang, 2013; Grabowski, 2020; Grabowski et al., 2022). The existence of such spatial and temporal variations prevents the interpretation of activation through the use of a single peak supersaturation value, as the critical supersaturation must be compared with a varying supersaturation field in both space and time.

https://doi.org/10.5194/egusphere-2026-3827
Preprint. Discussion started: 21 July 2026

Data collected by aircraft provide detailed but limited snapshots of clouds, whereas vertically oriented cloud radars provide continuous time–height sampling and strong sensitivity to the large-drop tail via Doppler spectra (e.g., Kollias et al., 2007; Rauber et al., 2007; Luke and Kollias, 2013; Radenz et al., 2019). Interpreting aerosol effects from radar alone has proved difficult because Doppler spectra combine microphysical properties with air motion and turbulence-induced broadening, as demonstrated by Feingold et al. (2003). Complementary process modeling is therefore needed.

To isolate the coupled roles of activation, mixing, and collision–coalescence under controlled dynamics, large-eddy simulations (LES) combined with a Lagrangian cloud model (LCM) based on the super-droplet method (LES–LCM) are utilized. Each super-droplet represents a multiplicity of real aerosol or droplet particles and is advected by the resolved turbulent flow. Microphysical evolution is integrated along each trajectory, so process attribution can rely on the full particle history rather than on instantaneous grid-mean states. The framework avoids numerical diffusion in spectral space and remains computationally tractable for shallow-cumulus studies (Shima et al., 2009; Arabas et al., 2015; Hoffmann et al., 2015; Grabowski et al., 2019; Maronga et al., 2020; Morrison et al., 2020).

Recent work has pushed LCM capabilities forward on several fronts. Graphics processing unit (GPU)-accelerated hybrid parallelization (Dziekan and Zmijewski, 2022) and algorithm optimizations for next-generation supercomputers (Matsushima et al., 2023) now make meter-scale cloud simulations with full Lagrangian microphysics feasible. Stochastic collision–coalescence in the super-droplet method produces lucky droplets that can trigger warm rain ahead of deterministic predictions (Dziekan and Pawlowska, 2017). Improvements in splitting and breakup algorithms extend the representable range of precipitation processes (Schwenkel et al., 2018; Unterstrasser et al., 2020; de Jong et al., 2023). An important process-level advance is the L3 framework (LES–LCM coupled to a linear eddy model), which assigns each super-droplet its own supersaturation perturbation and thereby resolves inhomogeneous mixing below the LES grid scale (Hoffmann et al., 2019). Applied to shallow cumulus, this approach shows that inhomogeneous mixing grows more prevalent as clouds mature and as aerosol loading or environmental dryness increases (Lim and Hoffmann, 2023, 2024). Multi-model benchmarks confirm that LCMs yield more realistic droplet spectra and precipitation onset than Eulerian bin schemes (Morrison et al., 2020; Chandrakar et al., 2022; Hill et al., 2023).

Because activation timing, entrainment exposure, and spectral broadening depend on the thermodynamic environment accumulated along individual trajectories rather than on instantaneous quantities averaged over a grid cell (Shaw, 2003; Grabowski and Wang, 2013; Grabowski et al., 2019), the Lagrangian framework is naturally suited to the questions pursued here. Realizing this potential in practice, however, requires two additional ingredients. One is a physically interpretable method for identifying relevant sub-populations, such as core versus entrained shell. The other is a mapping from microphysics represented at the level of individual particles to radar observables that enables direct evaluation against measurements.

In model–observation comparison, an increasingly important strategy is to compare radar quantities obtained from forward modeling directly with the measurements, rather than to force observations into model variables that the instrument does not directly measure. A radar forward operator translates the simulated drop population into equivalent radar reflectivity factors, Doppler moments, and Doppler spectra, allowing simulations that resolve the relevant processes to be evaluated against radar data in a physically consistent manner (Bohren and Huffman, 1983; Mech et al., 2020; Oue et al., 2020). For warm-rain studies,

https://doi.org/10.5194/egusphere-2026-3827
Preprint. Discussion started: 21 July 2026

this link is especially valuable, because radar reflectivity is dominated by the large-drop tail that bulk condensate diagnostics may fail to capture.

Despite extensive work on aerosol–warm-rain sensitivity in shallow cumulus, two gaps limit process attribution and observational evaluation. First, activation in turbulent shallow cumulus is still often assessed through diagnostic activated number or peak-supersaturation concepts, although droplets experience intermittent supersaturation and require finite time to grow beyond the Köhler critical radius. As a result, the timing distribution of activation, including its dependence on entrainment exposure, remains poorly constrained at the trajectory level. Second, observational inference is typically based on radar moments of low order, which combine microphysics with air motion and sampling effects, while the Doppler-spectral signature of aerosol-driven pathway changes is rarely linked back to activation histories in a framework that resolves individual particles. Previous LES–LCM studies examined warm-rain formation pathways, aerosol-to-activation evolution, and mixing effects in shallow cumulus, but explicit partitioning of trajectory sub-populations based on relative humidity (RH) history was not part of those analyses (Hoffmann et al., 2017, 2019; Lim and Hoffmann, 2023; Oh et al., 2023; Lim and Hoffmann, 2024). The present study addresses these gaps through three linked steps. Probability density functions (PDFs) and cumulative distribution functions (CDFs) of activation time are constructed along Lagrangian droplet histories, with all statistics weighted by multiplicity, and are interpreted by regimes identified from RH history. This makes finite-time activation directly diagnosable at the trajectory level. Clustering by RH history and diagnostics of mixing episodes across the whole population are then combined to separate core-like and entrained-shell pathways and to determine how activation closure biases depend on thermodynamic regime. The evolving particle population is finally translated into quantities that a radar would observe with a Ka-band forward operator applied directly to the particles. This allows a test of whether those aerosol-dependent pathway shifts remain visible in Doppler spectra.

This study combines controlled aerosol-loading experiments in LES–LCM with Lagrangian diagnostics using RH history and Ka-band radar forward modeling. Three idealized shallow-cumulus simulations, T13 (clean), T53 (intermediate), and T73 (polluted), are conducted using the Parallelized Large-Eddy Simulation Model (PALM) coupled to a super-droplet LCM, with the aerosol size-distribution shape held fixed while scaling total number concentration (Shima et al., 2009; Maronga et al., 2020). Persistent particle identifiers allow reconstruction of droplet histories from super-droplet trajectories, with all statistics weighted by multiplicity. Trajectories are clustered by RH history to separate core-like and entrained-shell pathways. A Ka-band forward operator applied directly to the particle population is then used to compute reflectivity, Doppler moments, and decomposed Doppler spectra.

The main objective is to trace how aerosol loading alters the pathway from activation to warm-rain formation in shallow cumulus and to test whether those pathway shifts leave identifiable signatures in Ka-band Doppler spectra. As a secondary diagnostic, activated droplet numbers for the individual clusters are compared to the Abdul-Razzak and Ghan (2000) parameterization to test whether a widely used equilibrium-based activation closure reproduces the aerosol- and regime-dependent activation behavior found in the LES–LCM diagnosis.

The present paper is organized as follows. Sect. 2 describes the model setup, diagnostic approaches, and radar forward operator. Results are presented in Sect. 3, following the causal sequence from aerosol loading through microphysical response

https://doi.org/10.5194/egusphere-2026-3827
Preprint. Discussion started: 21 July 2026

to radar-observable signatures. The analysis spans Eulerian condensate evolution, Lagrangian activation and growth diagnostics with clustering by RH history, mixing-episode characterization, and Ka-band Doppler-spectral forward modeling. Sect. 4 places the findings in the context of finite-time activation constraints in short-lived shallow cumulus and examines activation-closure biases and the potential of spectral structure as an observational constraint. The main conclusions are summarized in Sect. 5.

2 Model and methods

This section describes the LES–LCM framework, the controlled aerosol-loading experiments, the Lagrangian trajectory diagnostics, and the Ka-band radar forward operator used in this study. The methodological choices are designed to isolate how aerosol-induced changes in activation timing and post-activation growth propagate into drizzle formation and radar signatures.

2.1 Model

The Parallelized Large-Eddy Simulation Model (PALM), version 6.0 (Maronga et al., 2020), is employed, coupled to a Lagrangian cloud model based on the super-droplet method (Shima et al., 2009; Arabas et al., 2015). The coupled framework resolves turbulent transport together with microphysics represented at the level of individual particles, which is essential when activation depends on intermittent supersaturation exposure and finite growth time. This coupled framework has been applied in previous studies to investigate aerosol entrainment and activation in shallow cumulus (Hoffmann et al., 2015), raindrop formation pathways (Hoffmann et al., 2017), inhomogeneous mixing effects via the L3 sub-grid model (Hoffmann et al., 2019; Lim and Hoffmann, 2023, 2024), aerosol-to-activation paths (Oh et al., 2023), and fog microphysics (Schwenkel and Maronga, 2020). The resolved turbulent flow advects computational particles (super-droplets), each representing a multiplicity of real aerosol/droplet particles. Each super-droplet carries its dry aerosol size and evolves by classical Köhler theory (Köhler, 1936; Pruppacher and Klett, 1997). The equilibrium saturation ratio over a solution droplet of wet radius r follows Eq. (1).

$$S_{\mathrm{eq}} = 1 + \frac{A}{r} - \frac{B}{r^3}, \tag{1}$$

where the curvature (Kelvin) term is $A = 2M_{\mathrm{w}}\sigma_{\mathrm{w}}/(RT\rho_{\mathrm{w}})$ and the solute (Raoult) term is $B = \nu\Phi_{\mathrm{s}}M_{\mathrm{w}}\rho_{\mathrm{s}}r_{\mathrm{dry}}^3/(\rho_{\mathrm{w}}M_{\mathrm{s}})$. Here M_{w} and ρ_{w} are the molar mass and density of water, R is the universal gas constant, T is temperature, σ_{w} is the surface tension of the solution–air interface, ν is the van 't Hoff dissociation factor, Φ_{s} is the osmotic coefficient, M_{s} is the solute molar mass, and r_{dry} is the dry aerosol radius. The aerosol is assumed to be NaCl ($M_{\mathrm{s}} = 0.0584\,\mathrm{kg\,mol^{-1}}$, $\rho_{\mathrm{s}} = 2165\,\mathrm{kg\,m^{-3}}$, $\nu = 2$). Surface tension is parameterized with a linear temperature dependence, $\sigma_{\mathrm{w}} = 0.0761 - 1.55\times10^{-4}\,(T - 273.15)\,\mathrm{N\,m^{-1}}$, so that the Kelvin term responds to local temperature variations. The Raoult term B is temperature independent. Solubility variations are neglected.

For a given ambient supersaturation below the critical value, the relevant equilibrium lies on the left side of the Köhler maximum. This subcritical branch is stable and haze-like, because small perturbations in droplet size are damped by the equilibrium response. The Köhler maximum defines the critical supersaturation and the corresponding critical radius r_{crit}. Once that maximum is crossed, this stabilizing feedback is lost. On the activated side, further growth lowers the equilibrium

https://doi.org/10.5194/egusphere-2026-3827
Preprint. Discussion started: 21 July 2026

saturation ratio and introduces a positive feedback that favors continued condensational growth. Crossing r_{crit} therefore marks a qualitative transition from haze-like equilibration to activated cloud-droplet growth.

Condensational growth and evaporation are integrated along each super-droplet trajectory, while collision–coalescence is treated stochastically following the super-droplet method (Shima et al., 2009).

2.2 Experimental Setup for LES–LCM

A maritime shallow-cumulus-topped boundary layer is simulated in a computational domain with dimensions $L_x \times L_y \times L_z = 1920\,\mathrm{m} \times 3840\,\mathrm{m} \times 3840\,\mathrm{m}$ and an isotropic grid spacing of $20\,\mathrm{m}$. The LES equations are integrated using a third-order Runge–Kutta scheme with fifth-order advection for momentum and scalars, and the pressure Poisson equation is solved using fast Fourier transform (FFT)-based methods (Maronga et al., 2020). Boundary conditions are periodic in the lateral directions. For scalars, Dirichlet conditions are applied at the surface and Neumann (zero-gradient) conditions at the model top. The thermodynamic background state follows the Barbados Oceanographic and Meteorological Experiment (BOMEX) LES intercomparison case (Siebesma et al., 2003), but the configuration is used here as an idealized environment in which large-scale forcing is suppressed and surface heat and moisture fluxes are prescribed as fixed lower-boundary conditions to isolate microphysical sensitivities. The surface sensible heat flux is set to $8 \times 10^{-3}\ \mathrm{K\,m\,s^{-1}}$ and the surface latent heat flux to $5.2 \times 10^{-5}\ \mathrm{m\,s^{-1}}$. The inversion height is approximately $1500\,\mathrm{m}$.

Here, x denotes the horizontal direction along which the imposed thermal is homogeneous, y the cross-thermal horizontal direction, and z the vertical direction. Convection is triggered by an x-homogeneous warm perturbation (a slab-like thermal). The potential temperature perturbation θ^* is given by

$$\theta^* = \theta_0^* \exp\left[-\left(\frac{y - y_{\mathrm{c}}}{a_{\mathrm{y}}}\right)^2 - \left(\frac{z - z_{\mathrm{c}}}{a_{\mathrm{z}}}\right)^2\right], \tag{2}$$

where the perturbation is centered at $y_{\mathrm{c}} = 1920\,\mathrm{m}$ and $z_{\mathrm{c}} = 150\,\mathrm{m}$, with horizontal and vertical radii of $a_{\mathrm{y}} = 200\,\mathrm{m}$ and $a_{\mathrm{z}} = 170\,\mathrm{m}$, respectively. The maximum temperature perturbation is set to $\theta_0^* = 0.2\,\mathrm{K}$.

Super-droplets are released $5\,\mathrm{min}$ after simulation start to avoid artifacts during the initial bubble rise. They are distributed randomly throughout the domain up to $z = 2800\,\mathrm{m}$ with an initial average spacing of $4.5\,\mathrm{m}$, yielding approximately 88 super-droplets per $20\,\mathrm{m}$ grid box (about 2.3×10^8 super-droplets in the released volume). To improve statistical sampling of collision–coalescence, the initial multiplicity of each super-droplet is perturbed by a random factor drawn uniformly from $[0.5, 1.5]$. No random-seed ensemble is performed here, so the reported results should be interpreted as a single stochastic realization. Dry aerosol sizes are sampled from a maritime size distribution (Table 1) and the total aerosol number concentration is scaled to define three aerosol-loading experiments. The three cases are T13 (clean, $N_{\mathrm{a}} = 100\,\mathrm{cm}^{-3}$), T53 (intermediate, $N_{\mathrm{a}} = 1000\,\mathrm{cm}^{-3}$), and T73 (polluted, $N_{\mathrm{a}} = 5000\,\mathrm{cm}^{-3}$). These short labels are used for brevity, while the clean/intermediate/polluted descriptors are used throughout the discussion for clarity. Case definitions and time steps are summarized in Table 2. The aerosol perturbation is therefore imposed by uniform number concentration scaling rather than by changing the modal radii or adding a distinct coarse mode. The relative shape of the large-aerosol tail remains the same across cases. The initial aerosol field is horizontally homogeneous so that differences among simulations arise primarily from aerosol loading and the subsequent tur-

https://doi.org/10.5194/egusphere-2026-3827
Preprint. Discussion started: 21 July 2026

bulent transport and mixing. This idealized shallow-cumulus configuration is closely related to that of Hoffmann et al. (2017). Both studies use a BOMEX-based thermodynamic background and a warm-bubble trigger to isolate microphysical controls in a short-lived shallow-cumulus life cycle. Hoffmann et al. (2017) initialized all super-droplets with the same dry radius ($r = 0.01\,\mu\mathrm{m}$), whereas the present study samples a maritime dry-aerosol size distribution and scales only its total number concentration across three loading levels. The additional difference most relevant here is that activation is diagnosed explicitly as finite-time growth beyond the Köhler critical radius, using persistent particle identifiers.

Table 1. Maritime aerosol size distribution adopted from Jaenicke (1988). Each mode is characterized by its number concentration N_i, mode radius $r_{\mathrm{a},i}$, and geometric standard deviation $\log\delta_i$. The listed concentrations define the relative modal shape. For each experiment the entire distribution is uniformly scaled so that $\sum_i N_i = N_\mathrm{a}$ (Table 2). The modal radii, geometric widths, and the mean dry aerosol size therefore remain unchanged across cases.

Mode	N_i [cm^{-3}]	$r_{\mathrm{a},i}$ [µm]	$\log\delta_i$
1	1.33×10^2	0.004	0.66
2	6.66×10^1	0.133	0.21
3	3.06×10^0	0.290	0.40

Table 2. Overview of LES–LCM cases with initial aerosol number concentration N_a, simulation end time, and time step Δt. The microphysical time step is reduced with increasing aerosol loading to maintain numerical stability of the condensation solver under stronger competition for water vapor (Grabowski et al., 2018; Dziekan et al., 2019).

Case	N_a [cm^{-3}]	End Time [s]	Δt [s]
T13 (clean)	100	1800	1.00
T53 (intermediate)	1000	1800	0.20
T73 (polluted)	5000	1800	0.05

All prognostic variables and diagnostics are stored in Hierarchical Data Format version 5 (HDF5). A distinctive feature of this study is that persistent particle identifiers are assigned to all initial super-droplets and stored together with particle properties at all output times in the HDF5 output. This design enables an end-to-end Lagrangian reconstruction from persistent particle identifiers. For the trajectory-conditioned diagnostics used below, particle IDs present at the final output time ($t = 1800\,\mathrm{s}$) are traced backward through earlier outputs. Early-time statistics therefore refer to that late-time particle set rather than to the full instantaneous particle population at each earlier time.

2.3 Lagrangian diagnostics of clustering and activation timing

Each trajectory is summarized by a three-component relative humidity (RH) feature vector comprising $\mathrm{RH}_\mathrm{start}$ (RH at activation), $\overline{\mathrm{RH}}$ (trajectory-mean RH), and RH_end (RH at the end of the trajectory). After standardization, trajectories are partitioned

https://doi.org/10.5194/egusphere-2026-3827
Preprint. Discussion started: 21 July 2026

with k-means clustering (MacQueen, 1967). Centroids are initialized with the k-means++ scheme, which spreads the initial centroids across feature space more effectively than purely random initialization. For each candidate value of k, clustering is repeated for 10 independent initializations ($n_{\text{init}} = 10$), each followed by at most 300 Lloyd iterations. The solution with the lowest inertia is retained. A fixed random seed (`random_state=42`) is used to make the cluster assignment reproducible for the same input data within the present analysis environment.

Candidate values of k are evaluated with the elbow method (Thorndike, 1953), using an inertia-reduction threshold of 20 %, together with the silhouette score (Rousseeuw, 1987) and the Calinski–Harabasz index (Calinski and Harabasz, 1974). These diagnostics support $k = 4$, which is adopted as a fixed choice in the present analysis. Clusters are ordered by decreasing $\overline{\text{RH}}$ and interpreted as (1) core, (2) diluted core, (3) transition zone, and (4) entrained shell. Additional clustering diagnostics and sensitivity tests are provided in the Supplement.

For each super-droplet, the activation delay time τ_{act} is defined as the elapsed time from simulation start to the first instance at which the wet radius exceeds the corresponding Köhler critical radius r_{crit} for its dry aerosol size. All activation-time statistics are weighted by super-droplet multiplicity to represent the physical droplet population. The empirical cumulative distribution function (CDF) of activation time, weighted by multiplicity, is given by Eq. (3).

$$F_{\text{act}}(t) = \frac{\sum_{i \in \mathcal{A}} W_i \, \mathbb{I}(\tau_{\text{act},i} \leq t)}{\sum_{i \in \mathcal{A}} W_i}, \tag{3}$$

Here $\mathcal{A}$ is the set of activated super-droplets, $\tau_{\text{act},i}$ is the activation time of super-droplet i, W_i is its multiplicity, and $\mathbb{I}$ is the indicator function. The activation supersaturation $S_{\text{act},i}$ equals the ambient supersaturation sampled at $\tau_{\text{act},i}$. The quantity $\widetilde{S}_{\text{act}}$ reported later is the median of $S_{\text{act},i}$ over $\mathcal{A}$, again weighted by multiplicity.

Activated droplet number concentrations for each cluster are compared to the Abdul-Razzak and Ghan (2000) parameterization (ARG2000), applied offline to thermodynamic conditions sampled from the simulations. ARG2000 is used as a physically based parcel closure because, unlike simpler empirical formulations such as Twomey (1959), it links activated droplet number explicitly to aerosol size distribution and sampled thermodynamic conditions through a peak-supersaturation framework. The comparison is diagnostic rather than a full multi-scheme intercomparison.

2.4 Ka-band radar forward operator

Reflectivity and Doppler moments in radar-equivalent form are computed from the super-droplet population using a forward operator applied directly to the particles, following the Passive and Active Microwave TRAnsfer tool, PAMTRA version 1.0 (Mech et al., 2020), with exact Mie scattering for spherical liquid droplets (Bohren and Huffman, 1983). A vertically pointing Ka-band radar is assumed with frequency $f_{\text{r}} = 35\,\text{GHz}$ (wavelength $\lambda_{\text{r}} \approx 8.56\,\text{mm}$).

Within each radar sampling volume (a model grid cell of volume $V_{\text{bin}} = \Delta x\,\Delta y\,\Delta z$, where $\Delta x = \Delta y = \Delta z = 20\,\text{m}$), the volume backscattering coefficient is

$$\eta_{\text{b}} = \frac{1}{V_{\text{bin}}} \sum_{p \in \text{bin}} W_p \, \sigma_{\text{b}}(D_p), \tag{4}$$

https://doi.org/10.5194/egusphere-2026-3827
Preprint. Discussion started: 21 July 2026

where W_p is the multiplicity (number of physical droplets represented by super-droplet p), D_p is the particle diameter, and σ_b is the Mie backscattering cross section. For the Doppler spectra analyzed later for individual grid cells, neighboring 3×3 horizontal grid cells are additionally aggregated to $60\,\mathrm{m}$ by $60\,\mathrm{m}$ columns, and particles are collected within a $\pm 10\,\mathrm{m}$ height band about the target level. The Mie routine returns both the backscattering and extinction cross sections for each partial wave order n with Mie coefficients a_n and b_n (Bohren and Huffman, 1983). The corresponding cross sections are

$$\sigma_\mathrm{b} = \frac{\lambda_\mathrm{r}^2}{4\pi} \left| \sum_{n=1}^{N} (2n+1)(-1)^n (a_n - b_n) \right|^2, \tag{5}$$

and the extinction cross section is

$$\sigma_\mathrm{ext} = \frac{\lambda_\mathrm{r}^2}{2\pi} \sum_{n=1}^{N} (2n+1)\, \Re(a_n + b_n), \tag{6}$$

where $\Re$ denotes the real part, and the series is truncated at $N = \lfloor x + 4x^{1/3} + 2 \rfloor$ with size parameter $x = \pi D_p / \lambda_\mathrm{r}$.

The linear equivalent radar reflectivity factor is

$$Z_\mathrm{e}^\mathrm{lin} = \frac{\lambda_\mathrm{r}^4}{\pi^5 |K_\mathrm{w}|^2}\, \eta_\mathrm{b}, \tag{7}$$

with $|K_\mathrm{w}|^2 = 0.93$ denoting the dielectric factor of liquid water at Ka band. The intrinsic reflectivity is reported in dBZ as

$$Z_\mathrm{e,int} = 10 \log_{10}\left(Z_\mathrm{e}^\mathrm{lin}\right). \tag{8}$$

For Doppler-spectral analysis, moment definitions are written in terms of Doppler spectral reflectivity density $S(v)$ in linear reflectivity units. The zeroth moment is

$$M_0 = \int S(v)\,\mathrm{d}v = Z_\mathrm{e}^\mathrm{lin}. \tag{9}$$

The mean Doppler velocity is

$$V_\mathrm{D} = \frac{\int v\, S(v)\,\mathrm{d}v}{M_0}. \tag{10}$$

The spectral width W follows from the second central moment,

$$W = \sigma_v = \left[\frac{\int (v - V_\mathrm{D})^2\, S(v)\,\mathrm{d}v}{M_0} \right]^{1/2}. \tag{11}$$

The spectral skewness is

$$\gamma = \frac{1}{\sigma_v^3} \frac{\int (v - V_\mathrm{D})^3\, S(v)\,\mathrm{d}v}{M_0}. \tag{12}$$

Positive γ indicates a tail toward positive velocities. Negative γ points toward more negative velocities, typically associated with larger, faster-falling hydrometeors.

https://doi.org/10.5194/egusphere-2026-3827
Preprint. Discussion started: 21 July 2026

To include propagation losses for a ground-based vertically pointing radar, two-way path-integrated attenuation is applied following the PAMTRA radar simulator (Mech et al., 2020). In each height bin i, the volume extinction coefficient is

$$k_{\mathrm{ext},i} = \frac{10^{-6}}{V_{\mathrm{bin}}} \sum_{p \in i} W_p \, \sigma_{\mathrm{ext}}(D_p), \quad [\mathrm{m}^{-1}] \tag{13}$$

where σ_{ext} is the Mie extinction cross section in mm^2 and the factor 10^{-6} converts to m^2. One-way hydrometeor attenuation per bin is

$$A_{\mathrm{hyd},i} = \frac{10}{\ln 10} \, k_{\mathrm{ext},i} \, \Delta h = 4.343 \, k_{\mathrm{ext},i} \, \Delta h, \quad [\mathrm{dB}] \tag{14}$$

where Δh is the bin thickness. Absolute temperature and water-vapor density are first computed from potential temperature, hydrostatic pressure, and specific humidity using standard thermodynamic relations. Gaseous attenuation due to O_2 and H_2O absorption is then estimated from these profiles with a simplified International Telecommunication Union Radiocommunication Sector (ITU-R) P.676 formulation (ITU-R, 2022). The corresponding bin-wise gaseous attenuation is

$$A_{\mathrm{gas},i} = 10^{-3} \, \alpha_{\mathrm{gas},i} \, \Delta h, \quad [\mathrm{dB}] \tag{15}$$

where $\alpha_{\mathrm{gas},i}$ is the specific gaseous attenuation [$\mathrm{dB\,km}^{-1}$].

For a radar at the lowest model level, the cumulative two-way path-integrated attenuation (PIA) to the center of range gate i is computed by bottom-up summation following PAMTRA and is given by

$$\mathrm{PIA}_i = 2 \sum_{j=1}^{i-1} \left(A_{\mathrm{hyd},j} + A_{\mathrm{gas},j} \right) + \left(A_{\mathrm{hyd},i} + A_{\mathrm{gas},i} \right), \quad [\mathrm{dB}] \tag{16}$$

where the factor of 2 accounts for the two-way path through bins below the target, while the target bin itself contributes only one-way attenuation because the scattering volume is located at its center.

In PAMTRA, attenuation is applied in the linear domain. The linear PIA factor is

$$\mathrm{PIA}_{\mathrm{lin},i} = 10^{0.1\,\mathrm{PIA}_i}, \tag{17}$$

and the attenuated linear reflectivity and Doppler spectrum are

$$Z^{\mathrm{lin}}_{\mathrm{e},i} = \frac{Z^{\mathrm{lin}}_{\mathrm{e,int},i}}{\mathrm{PIA}_{\mathrm{lin},i}}, \qquad S_{\mathrm{att}}(v) = \frac{S(v)}{\mathrm{PIA}_{\mathrm{lin},i}}. \tag{18}$$

Because division in the linear domain is equivalent to subtraction in the logarithmic domain, the attenuated reflectivity in dBZ is simply

$$Z_{\mathrm{e},i}\,[\mathrm{dBZ}] = Z_{\mathrm{e,int},i}\,[\mathrm{dBZ}] - \mathrm{PIA}_i\,[\mathrm{dB}]. \tag{19}$$

Since PIA is a uniform multiplicative factor across the velocity axis, the Doppler moments V_{D}, W, and γ are unaffected by attenuation and remain identical to their intrinsic values. In the remainder of this paper, Z_{e} denotes attenuated reflectivity unless stated otherwise.

https://doi.org/10.5194/egusphere-2026-3827
Preprint. Discussion started: 21 July 2026

For the radar-mode decomposition and drizzle summary presented later, droplets with $r < 40\,\mu\mathrm{m}$ are assigned to the cloud mode, and droplets with $r \geq 40\,\mu\mathrm{m}$ define the drizzle/rain mode. For grid cells containing drizzle-class droplets, the reflectivity–rain-rate relationship is diagnosed in the canonical power-law form $Z_\mathrm{e}^\mathrm{lin} = a_\mathrm{ZR} R^{b_\mathrm{ZR}}$, where $Z_\mathrm{e}^\mathrm{lin}$ is the attenuated equivalent radar reflectivity factor in linear units and R is the corresponding model rain rate. The coefficients a_ZR and b_ZR are obtained at each analysis time by ordinary least-squares regression in log space.

https://doi.org/10.5194/egusphere-2026-3827
Preprint. Discussion started: 21 July 2026

3 Results

Results are organized along the pathway from aerosol loading through microphysical response to radar-observable signatures. Eulerian condensate evolution first identifies the bulk stages of cloud growth, maturity, and decay, providing the temporal framework for the later diagnostics based on trajectories (Sect. 3.1). Lagrangian growth diagnostics and clustering by RH history then quantify pathway differences among sub-populations (Sects. 3.2–3.3). Mixing-episode and activation-time analyses address entrainment-driven processes and parameterization biases (Sect. 3.4). Ka-band forward modeling maps these differences onto quantities that a radar would observe (Sect. 3.5). Additional diagnostics and figures are collected in the Supplement.

These subsections are not intended as separate topics. Physical interpretation is developed throughout the Results and is then synthesized in Sect. 4. The early results establish how aerosol loading modifies activation, growth after activation, and the precipitation-mode tail. The later subsections then examine whether the same pathway differences appear in a diagnostic activation closure and in quantities that a radar would observe.

3.1 Spatio-temporal distribution of cloud liquid water

Cloud liquid water shows only modest aerosol sensitivity in this Eulerian view. The decomposition therefore provides life-cycle context for the more aerosol-sensitive microphysical diagnostics that follow. To distinguish whether the modest aerosol-driven changes in condensate averaged over the domain arise from differences in geometric occupancy or in the water content inside clouds, the vertical distribution of cloud liquid water q_l is decomposed into three components (Fig. 1). The horizontal mean $\overline{q_\mathrm{l}}(z)$, cloudy-area fraction $f_\mathrm{c}(z)$, and mean $\langle q_\mathrm{l}\rangle_\mathrm{cld}(z)$ within cloudy air are evaluated separately, with cloudy grid cells defined by $q_\mathrm{l} > 0.01\,\mathrm{g\,kg^{-1}}$ (Siebesma and Cuijpers, 1995; Siebesma et al., 2003; Korolev et al., 2007; van Zanten et al., 2011). In this single-cloud setup, $f_\mathrm{c}(z)$ should be interpreted as a domain-relative occupancy measure rather than as a cloud-field statistic.

Early on ($t = 820\,\mathrm{s}$), $q_\mathrm{l}(z)$ peaks weakly near cloud base ($\sim$650 m to 800 m) and cloudy-area fractions are small. The three cases look similar initially. By the intensification stage ($t = 1220\,\mathrm{s}$), that changes. Horizontal-mean condensate increases with aerosol loading (peak $\overline{q_\mathrm{l}}$ increases from $\sim 0.08\,\mathrm{g\,kg^{-1}}$ in T13 to $\sim 0.10\,\mathrm{g\,kg^{-1}}$ in T73), because of larger $f_\mathrm{c}(z)$ in the polluted case. The in-cloud mean $\langle q_\mathrm{l}\rangle_\mathrm{cld}(z)$, by comparison, differs less between experiments. Later ($t = 1620\,\mathrm{s}$), condensate decreases and the q_l peak shifts upward ($\sim$1.4 km to 1.6 km). The inter-case ordering is no longer monotonic. T13 now has the largest aloft peak, T73 the smallest. This reversal reflects the combined effect of activation timing and post-activation growth rate. In the clean case, earlier activation and faster diffusional growth allow droplets to reach larger sizes before being transported aloft, so that T13 sustains a higher in-cloud condensate at upper levels. In the polluted case, delayed activation and stronger competition for water vapor keep droplets smaller and the condensate peak weaker. Because only one thermally triggered cloud is sampled, late-stage differences in $f_\mathrm{c}(z)$ also reflect geometric intermittency of the evolving cloud within the finite domain. The weak bulk sensitivity here, contrasted with the stronger microphysical sensitivity documented below, is in line with buffered aerosol responses in warm shallow clouds (Stevens and Feingold, 2009; Hoffmann et al., 2017; Oh et al., 2023). Cross-sections of the evolving condensate geometry appear in Fig. S1. The non-monotonic late-stage condensate response cannot be explained from the Eulerian decomposition alone. Identifying which droplet sub-populations activate early, broaden

https://doi.org/10.5194/egusphere-2026-3827
Preprint. Discussion started: 21 July 2026

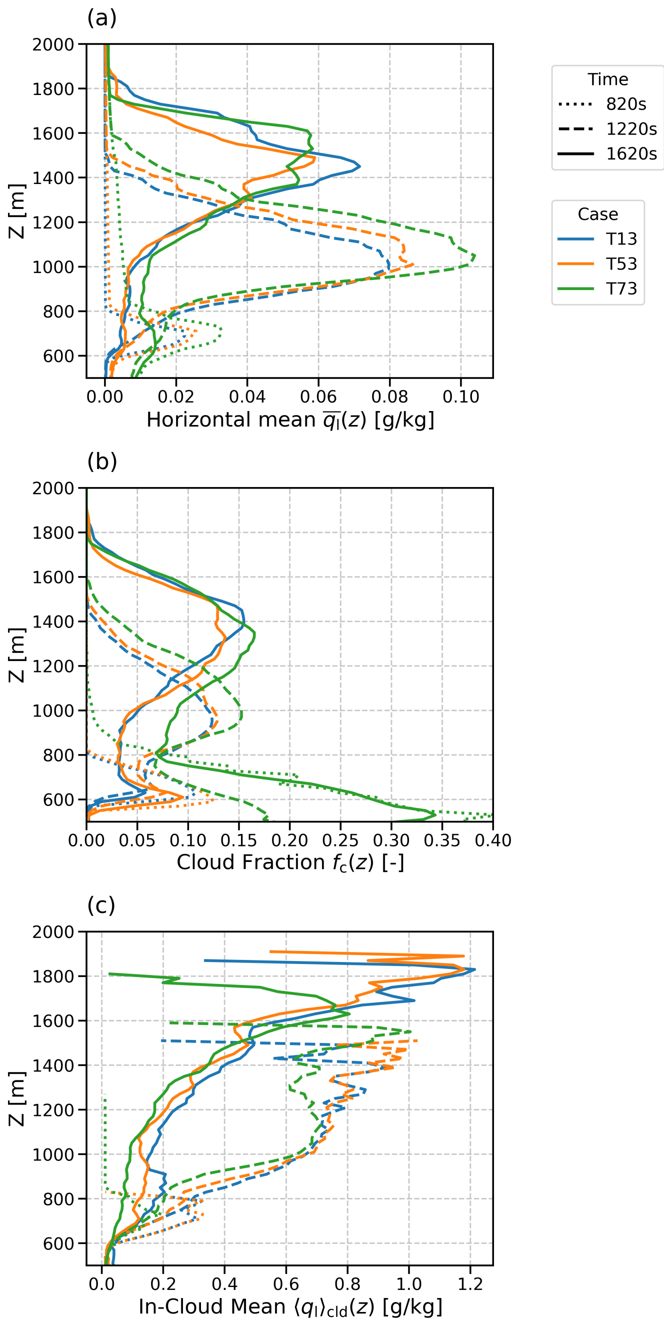

Figure 1. Life-cycle context from the vertical distribution of cloud liquid water mixing ratio. (a) Horizontal mean $\overline{q_l}(z)$. (b) Domain-relative cloudy-area fraction $f_c(z)$ within the finite model domain, defined from grid cells satisfying $q_l > 0.01\ \mathrm{g\,kg^{-1}}$. (c) In-cloud mean $\langle q_l \rangle_{cld}(z)$ computed over the same cloudy subset. Line styles denote time, with dotted, dashed, and solid lines corresponding to 820 s, 1220 s, and 1620 s, respectively. Colors denote aerosol cases. Blue corresponds to T13, orange to T53, and green to T73.

https://doi.org/10.5194/egusphere-2026-3827
Preprint. Discussion started: 21 July 2026

spectrally, and feed (or fail to feed) the precipitation-mode tail requires tracking individual particle histories, as described in the following subsections.

3.2 Growth and drizzle diagnostics from trajectories

Tracked super-droplet histories retained in the LES–LCM output (Sect. 2.3) connect the condensate picture to warm-rain pathway development. Using $t_0 = 600\,\mathrm{s}$ as a common reference time and $r_0 = r(t_0)$ as the corresponding wet radius, Fig. 2 summarizes this growth problem from three complementary angles. Panel (a) shows how fast tracked trajectories grow after t_0, quantified by the mean growth rate over the analyzed interval beginning at t_0 and plotted against r_0. Panel (b) shows how much each trajectory grows over the analyzed interval, expressed by the maximum-growth ratio $G \equiv \Delta r / r_0$, together with the normalized time at which that maximum is reached, $t^*_{r_{\max}} = [t(r_{\max}) - t_0]/(t_{\mathrm{end}} - t_0)$. Values of $t^*_{r_{\max}}$ close to 1 indicate that the maximum radius is reached late in the analyzed interval. Panel (c) shows how often trajectories reach drizzle-relevant size, expressed as the drizzle-occurrence fraction for trajectories exceeding $r = 40$ µm. This threshold is chosen for consistency with the cloud–rain partition used for the radar spectral decomposition in Sect. 3.5 and with commonly used warm-rain thresholds (Khairoutdinov and Kogan, 2000; Seifert and Beheng, 2001). Related super-droplet simulations show that the emergence of droplets larger than $r = 40\,\mathrm{\mu m}$ marks the onset of rapid collisional growth in shallow cumulus (Hoffmann et al., 2017).

The aerosol dependence is clear. In Fig. 2(a) and (b), each dot denotes one trajectory-level summary in which rapid growth appears, and the upper tail is more informative than a bulk mean alone. At larger r_0, the upper envelope of the mean growth rate in Fig. 2(a) is highest in T13 and progressively reduced in T53 and T73. Fewer rapid-growth trajectories are available to seed collision–coalescence in T73. Large net-growth ratios G (Fig. 2b) show a similar pattern, occurring more frequently and reaching larger magnitudes in T13, while the polluted case clusters toward smaller G values. This emphasis on the upper tail aligns with previous Lagrangian warm-rain studies showing that a limited subset of rapidly growing droplets preconditions the onset of efficient collisional growth (Grabowski and Wang, 2013; Hoffmann et al., 2017). Note that the fraction of tracked super-droplet trajectories reaching drizzle-relevant size ($r \geq 40\,\mathrm{\mu m}$) drops from 20.1 % (T13) to 15.3 % (T53) and 15.0 % (T73) (Fig. 2c). This is not a surface-precipitation efficiency, but it serves as a useful proxy for how readily the large-drop tail develops (see Fig. S2 for the full G distribution). Clustering by RH history is used next to separate physically distinct sub-populations and identify which regimes contribute most to the rapid-growth tail.

3.3 Clustering of super-droplet moisture histories

Population-level growth metrics lump together trajectories from localized regions of the cloud that experience very different entrainment and humidity histories. Distinguishing these sub-populations is essential for understanding which growth pathways contribute to the precipitation-mode tail and which do not. A clustering approach is therefore applied to address this challenge. Applying the clustering method based on RH history described in Sect. 2.3 yields four regimes (Table 3). The adopted choice $k = 4$ reflects a compromise among standard internal metrics (Fig. S3) and the physical interpretability of the resulting regimes. The labels assigned to these regimes (adiabatic-core-like, diluted-core-like, transition-zone-like, and entrained-shell-like) serve as physically motivated descriptors rather than definitive dynamical classifications. The analysis that follows traces how each

https://doi.org/10.5194/egusphere-2026-3827
Preprint. Discussion started: 21 July 2026

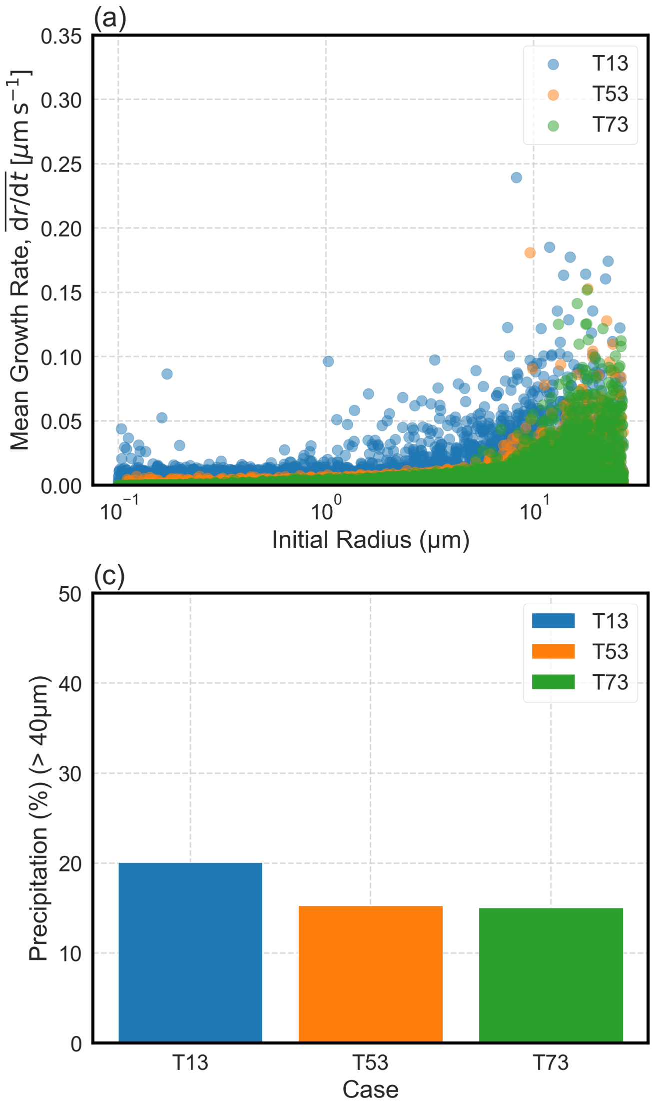

Figure 2. Growth diagnostics based on trajectories for T13, T53, and T73. (a) Mean growth rate over the analyzed interval beginning at t_0 versus initial wet radius $r_0 = r(t_0)$, with $t_0 = 600\,\mathrm{s}$. (b) Maximum-growth ratio $G \equiv \Delta r / r_0$ versus normalized time $t^*_{r_\mathrm{max}}$ at which the maximum radius is reached, where $t^*_{r_\mathrm{max}} = 1$ corresponds to the end of the analyzed interval. In both panels, each dot represents one tracked trajectory. (c) Drizzle-occurrence fraction for trajectories exceeding $r = 40\,\mathrm{\mu m}$. The scatter representation in panels (a) and (b) is retained to expose the upper envelope and the rare rapid-growth trajectories that contribute to the precipitation-mode tail.

https://doi.org/10.5194/egusphere-2026-3827
Preprint. Discussion started: 21 July 2026

Table 3. Summary of the four cluster regimes identified from RH history and used in the trajectory analysis. The cluster numbering follows the classification derived from RH history introduced in Sect. 2.3 and used throughout Sect. 3.3.

Cluster	Regime
1	adiabatic-core-like
2	diluted-core-like
3	transition-zone-like
4	entrained-shell-like

regime responds to aerosol loading through presentation and discussion of moisture-history diagnostics, size-distribution evolution, activation-time statistics, and parameterization biases.

3.3.1 T13: clean conditions

In the clean T13 case (Fig. 3), the separation between the clusters is striking. The adiabatic-core cluster (Cluster 1) attains the highest peak RH and sustains conditions most favorable for growth (panel a), while the entrained-shell cluster (Cluster 4) remains systematically drier and relaxes more slowly toward saturation. Panel (b) shows the corresponding wet-radius evolution in absolute time for the clusters identified from RH history. No activation filter is applied, so the cluster means include both activated droplets and subcritical haze particles. The displayed trajectories are defined from particle IDs present at $t = 1800\,\mathrm{s}$ and traced backward through earlier outputs. Early in the simulation, the transition-zone cluster (Cluster 3) and the entrained-shell cluster (Cluster 4) begin from slightly larger wet radii than the adiabatic-core and diluted-core clusters (Clusters 1 and 2). This offset likely reflects preferential loss of the smallest particles from Clusters 3 and 4 before $t = 1800\,\mathrm{s}$ under the drier shell-like conditions. Backward reconstruction from the final particle set therefore shifts the early-time mean toward somewhat larger radii. The radius excess near $t = 0$ should not be interpreted as an initial size advantage of the shell-like clusters.

Later, the adiabatic-core cluster (Cluster 1) overtakes the shell-like clusters and reaches the largest radii. The diluted-core cluster (Cluster 2) falls in between, and its elevated RH variability (panel c) points to intermittent mixing in otherwise moist air. The transition cluster (Cluster 3) falls between the diluted-core cluster (Cluster 2) and the entrained-shell cluster (Cluster 4). Radius variability (panel d) decreases from core-like to shell-like clusters, with the entrained-shell regime exhibiting the smallest spread.

Panels (e) and (f) relate the clusters identified from RH history to the spatial sampling of the trajectories. Because the initiating warm perturbation is homogeneous in the x direction, meaningful horizontal structure is expected primarily across the cloud in y. In panel (e), p_y therefore denotes the mean horizontal trajectory position evaluated over the portion of each trajectory after $t = 720\,\mathrm{s}$, a cutoff that falls close to the cluster-mean RH peak in panel (a) for most clusters. Substantial overlap remains, as expected in a turbulent cloud. Yet the higher-RH subsets are populated preferentially by the adiabatic-core and diluted-core clusters (Clusters 1 and 2), whereas the lower-RH subsets extend more often into laterally displaced p_y branches associated with the entrained-shell cluster (Cluster 4). Panel (f) summarizes residence in percentile-defined peripheral regions.

https://doi.org/10.5194/egusphere-2026-3827
Preprint. Discussion started: 21 July 2026

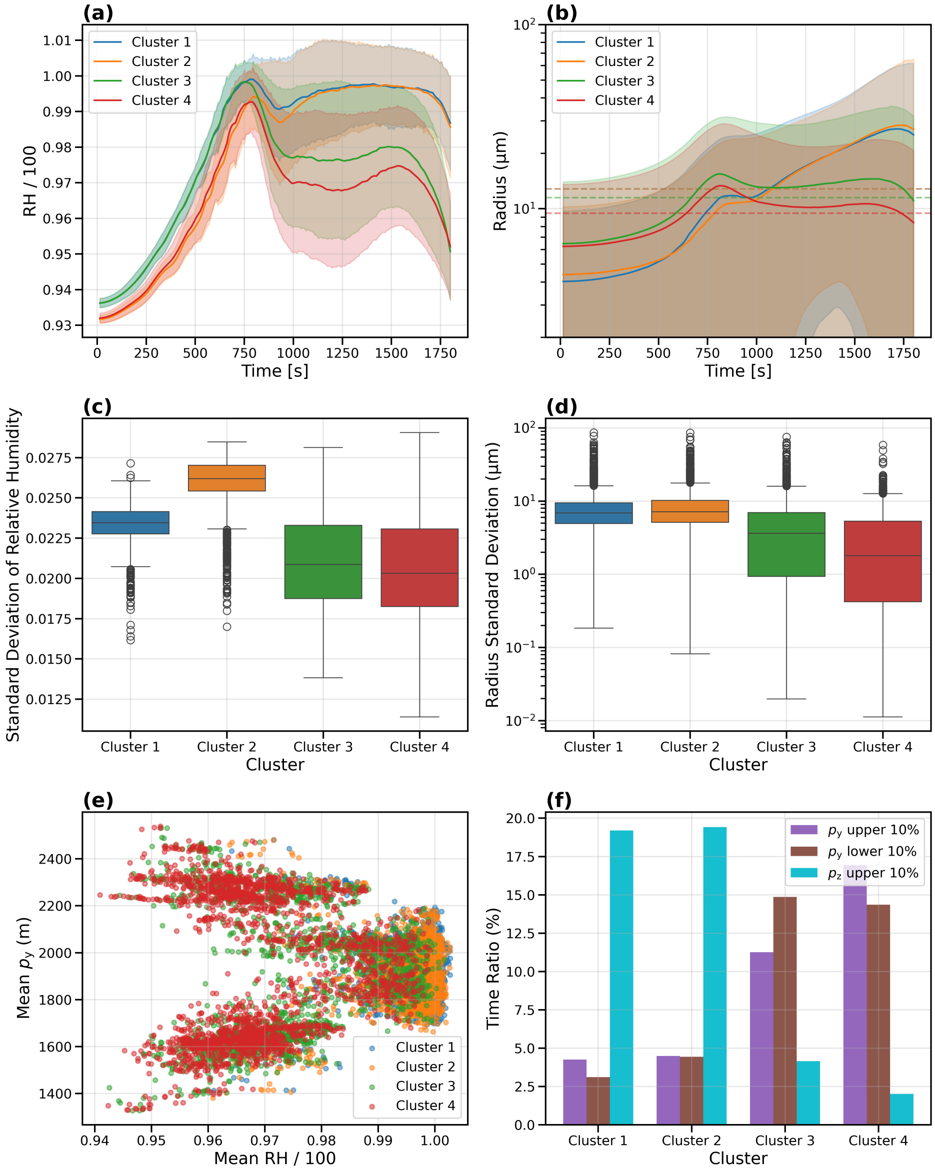

Figure 3. Cluster-wise moisture-history diagnostics for T13. Cluster colors are ordered from the adiabatic-core-like regime (Cluster 1) to the entrained-shell-like regime (Cluster 4). (a) Mean relative humidity (RH) and (b) mean wet radius versus absolute time since simulation start. Shading indicates $\pm 1\sigma$ across trajectories. The trajectory set is defined from particle IDs present at $t = 1800\,\mathrm{s}$ and reconstructed backward in time. Early-time means in panel (b) therefore refer to that late-time particle set and can be shifted high if the smallest particles in the drier clusters are preferentially lost before the final output. Panel (b) includes both activated droplets and subcritical haze particles within the analyzed clusters identified from RH history. (c) Distribution of the within-trajectory standard deviation of RH. (d) Distribution of the within-trajectory standard deviation of radius. (e) Mean RH versus the mean horizontal trajectory position p_y, evaluated over the later part of each trajectory. (f) Fraction of time spent in percentile-defined peripheral regions. Here p_y and p_z denote the horizontal and vertical trajectory positions, respectively. Saturation corresponds to $\mathrm{RH} = 1$.

https://doi.org/10.5194/egusphere-2026-3827
Preprint. Discussion started: 21 July 2026

The upper and lower 10 % of the horizontal position p_y represent the two lateral edge zones, while the upper 10 % of the vertical position p_z denotes the upper part of the sampled vertical range. The entrained-shell cluster (Cluster 4) spends the most time in these edge-related regions, while Clusters 1 and 2 remain there less often. Taken together, panels (e) and (f) indicate that the classification derived from RH history carries a weak but physically meaningful spatial organization, even though turbulent mixing prevents any sharp boundary between core-like and shell-like regions. This spatial correspondence broadly aligns with the cloud-base (CB) and entrained-above (EA) aerosol categories introduced by Hoffmann et al. (2015) and applied by Oh et al. (2023), where CB aerosols enter at cloud base and EA aerosols are entrained laterally above it.

3.3.2 T73: polluted conditions

The same ordering holds in the polluted T73 case (Fig. S4), but the spread is compressed. Peak RH excursions are lower in T73 than in T13, reflecting stronger competition for water vapor under elevated CCN. At the same time, T73 trajectories remain closer to saturation for longer after the peak, a pattern driven by the more gradual moisture adjustment of the numerous small droplets. Radius variability is also compressed under higher aerosol loading, matching the reduced upper envelope of the mean growth rate and the smaller G values reported in Fig. 2. With distinct humidity exposures now assigned to each cluster, the question is how these regime differences appear in the evolving droplet size distribution and in the emergence or suppression of a collector-drop tail.

3.3.3 Impacts on particle spectrum

Whether the humidity differences among clusters translate into measurable changes in the particle spectrum is tested with size distributions of wet particles examined separately for each cluster in Fig. 4. The spectra are plotted against the diameter of wet particles, D. Solid lines show the full number-based spectra, dN/dD, including both subcritical particles and activated droplets. Dashed lines and shaded areas denote the activated subset defined by $r > r_{\text{crit}}$. The initial dry aerosol distribution is entirely submicron (Table 1), so particles with large wet diameters must have formed during the simulation rather than being inherited from the initial condition. Comparison with the whole-cloud or in-cloud mass-density spectra reported by Hoffmann et al. (2017) and Oh et al. (2023) therefore requires care.

At $t = 1000\,\text{s}$ during the development stage, the inter-case contrasts are concentrated at small diameters. T73 shows elevated concentrations for $D \approx 1$–10 µm in every cluster because more CCN compete for vapor and condensational growth proceeds more slowly. The majority of these particles are subcritical haze, not activated droplets. Because the dry aerosol size distribution includes a coarse-mode tail (Table 1), aerosols with larger dry radii undergo substantial hygroscopic growth, swelling to wet diameters of several micrometers even when the ambient supersaturation remains below their critical value. Under the suppressed supersaturation of T73, many of these particles never cross r_{crit} and therefore persist as unactivated haze rather than entering sustained cloud-droplet growth. Although their wet sizes are large, the number concentration of such subcritical particles remains too low to accelerate collision–coalescence appreciably. In the collector-drop range ($D \gtrsim 40$ µm), where collision–coalescence becomes efficient, the three cases remain nearly indistinguishable at this stage. Although a very sparse tail extending beyond $D \gtrsim 80$ µm already appears in T73 Clusters 3 and 4, its concentration stays near $10^{-6}\ \text{cm}^{-3}\,\mu\text{m}^{-1}$, too

https://doi.org/10.5194/egusphere-2026-3827
Preprint. Discussion started: 21 July 2026

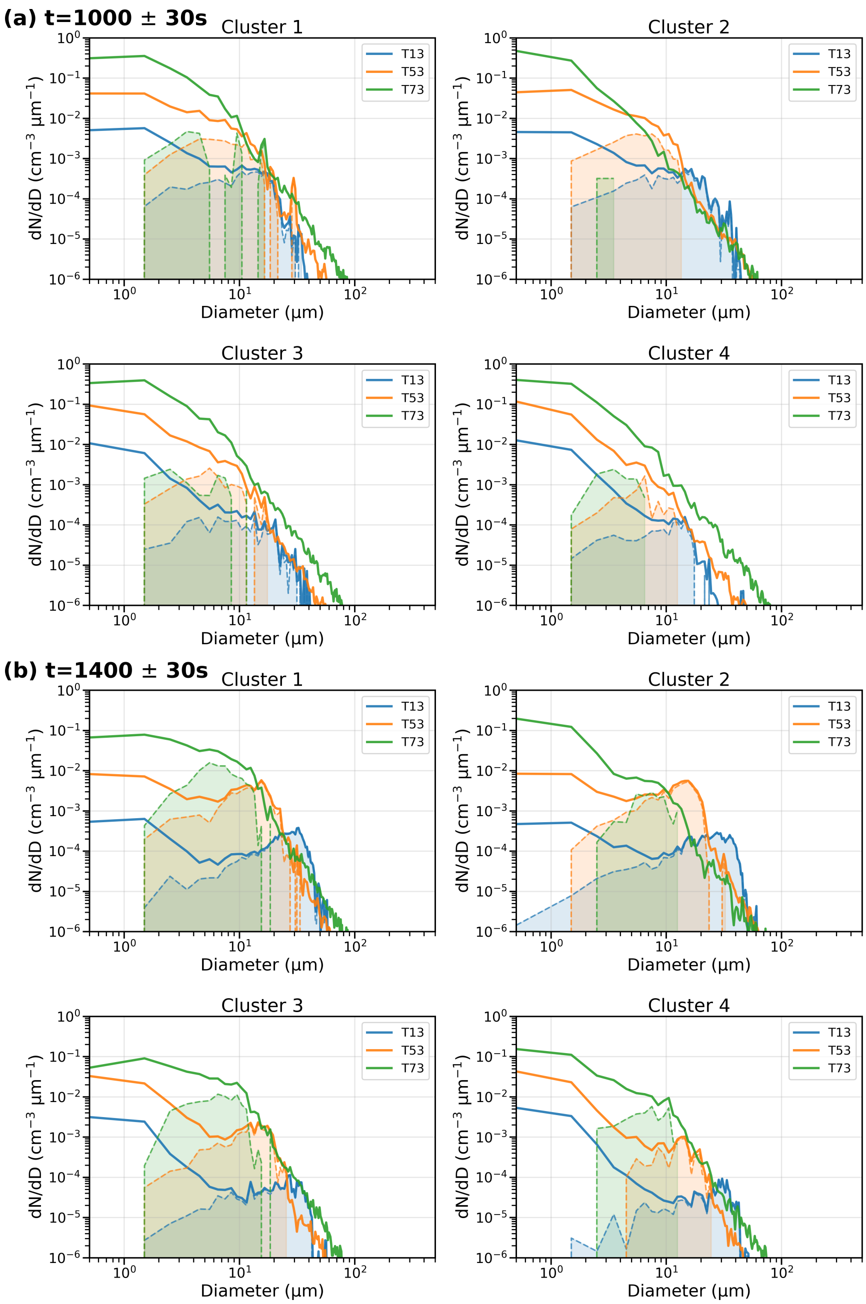

Figure 4. Size distributions of wet particles for each cluster in T13, T53, and T73. The horizontal axis shows the diameter of wet particles, D. Solid lines denote all particles (subcritical and activated). Dashed lines and shaded areas denote the activated subset ($r > r_{\mathrm{crit}}$). Panels (a) and (b) correspond to time windows centered at $t = 1000\,\mathrm{s}$ and $t = 1400\,\mathrm{s}$, using super-droplets sampled within $\pm 30\,\mathrm{s}$ of each time. Within each group, the four panels show Clusters 1–4. At a given time, each spectrum includes all super-droplets assigned to that cluster across the full domain.

https://doi.org/10.5194/egusphere-2026-3827
Preprint. Discussion started: 21 July 2026

low to contribute measurably to bulk liquid mass or to accelerate collisional growth. At this early time, the aerosol perturbation therefore shapes the cloud-droplet mode but has not yet produced the collector-drop tail separation that emerges by $t = 1400\,\mathrm{s}$.

The mature stage at $t = 1400\,\mathrm{s}$ is where the differences are most pronounced. T13 develops a secondary peak in the collector-drop range around $D \sim 20\,\mathrm{\mu m}$ to $50\,\mathrm{\mu m}$, especially in the adiabatic-core cluster (Cluster 1) and the diluted-core cluster (Cluster 2). This separation deserves emphasis because collision–coalescence is accelerated once such a collector-drop subpopulation emerges beside the more numerous small droplets. The resulting size contrast increases differential fall speeds and collection efficiency (Pruppacher and Klett, 1997; Hoffmann et al., 2017). Under a closely related shallow-cumulus setup, Hoffmann et al. (2017) showed that the earliest collisional growth is concentrated near cloud top. Cluster 1 sustains the highest mean supersaturation. Cluster 2 experiences intermittent entrainment that can locally enhance supersaturation fluctuations, allowing a similarly extended collector-drop branch. This interpretation is consistent with Fig. 3(f), where Clusters 1 and 2 spend the largest fraction of time in the upper 10 % of the sampled vertical trajectory range and therefore align most closely with the cloud-top region identified by Hoffmann et al. (2017).

The contrast with T73 is especially clear in panel (b). Many T73 particles with wet diameters above about $D = 20\,\mathrm{\mu m}$ remain outside the activated subset. This separation between the full and activated spectra suggests that subcritical particles can attain substantial wet sizes without entering sustained post-critical growth when supersaturation remains weak and intermittent. Once droplets cross r_{crit}, continued condensational growth is more readily sustained during supersaturated periods. T73 therefore lacks the secondary peak evident in Clusters 1 and 2 of T13 and instead shows a weaker, less extended upper tail. In Clusters 3 and 4, a bimodal structure is not evident and the upper tail remains short and sparse. The RH and DSD diagnostics reinforce each other. Higher aerosol loading promotes a more numerous but narrower droplet population and reduces the frequency of trajectories undergoing rapid condensational broadening. Across clusters, this condensational bottleneck limits transfer of activated droplets into the collector-size range where collision kernels increase rapidly. The weaker activated upper tail in T73 matches the reduced drizzle-occurrence fraction (20.1 % $\rightarrow$ 15.0 %) documented in Fig. 2. These results suggest that delayed activation alone does not explain the weak activated upper tail in T73. Continued condensational growth after activation is also required to build the collector-drop tail that precedes efficient collisional growth, in line with pathway analyses in shallow cumulus (Hoffmann et al., 2017; Oh et al., 2023). Before turning to the mixing-episode analysis that quantifies the entrainment-evaporation pathways behind this spectral narrowing, the activation-time distributions are examined to determine how aerosol loading controls the temporal onset of droplet growth.

3.3.4 Impacts on activation timing

In short-lived shallow cumulus, the time window available for collision–coalescence is tightly constrained by the convective life cycle (Heus et al., 2009; Hoffmann et al., 2017). Activation timing therefore controls how much growth time remains before the cloud dissipates. Activation-time PDFs and CDFs (Fig. 5) are constructed for each aerosol regime and each cluster. Higher aerosol loading delays activation. The shift is substantial. Mean activation time rises from $967\,\mathrm{s}$ (T13) to $1084\,\mathrm{s}$ (T53) and $1268\,\mathrm{s}$ (T73), while median activation supersaturation drops from 0.29 % to 0.12 % and 0.07 % (Table 4). These two shifts reflect different aspects of the aerosol response. The lower median activation supersaturation means that the activated subset

https://doi.org/10.5194/egusphere-2026-3827
Preprint. Discussion started: 21 July 2026

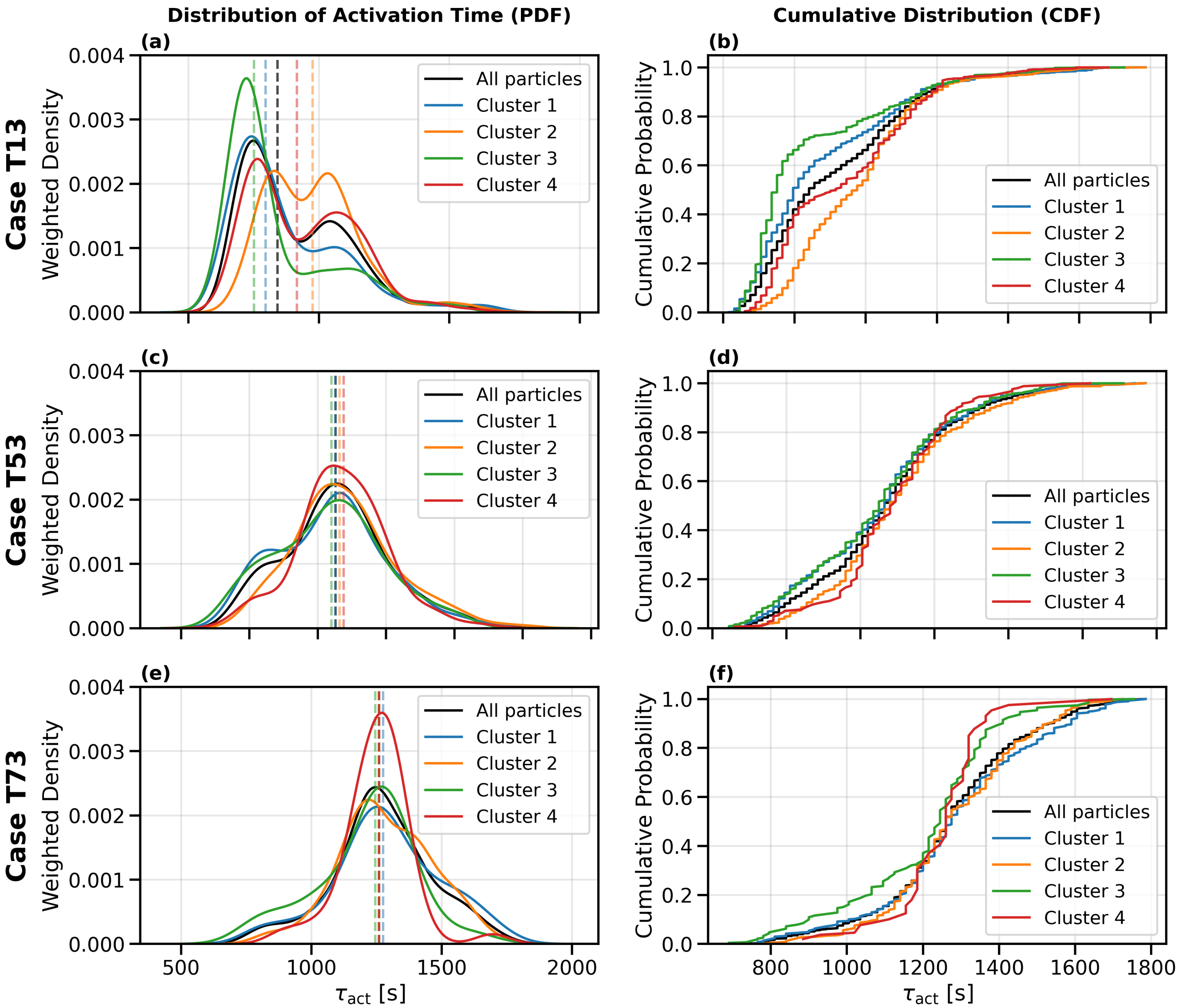

Figure 5. Multiplicity-weighted activation-time distributions for T13, T53, and T73. The left column (a, c, e) shows the probability density function (PDF). The right column (b, d, f) shows the cumulative distribution function (CDF). Rows correspond to T13 (top), T53 (middle), and T73 (bottom). Vertical dashed lines indicate cluster-wise mean activation times. Colors designate clusters identified from RH history. The polluted case (T73) shows delayed and more synchronized activation.

is dominated by particles with lower critical supersaturation, which implies smaller activated droplet sizes. The longer mean activation time shows that even these particles reach r_{crit} later, because favorable supersaturation is weaker and shorter-lived.

The shape of the activation-time PDF changes qualitatively across aerosol regimes. In T13, the full-population PDF is bimodal, with two temporally separated activation episodes and substantial separation among the distributions for the individual

https://doi.org/10.5194/egusphere-2026-3827
Preprint. Discussion started: 21 July 2026

Table 4. Summary of activation statistics for each case. Columns report the mean activation time $\bar{\tau}_{\mathrm{act}}$ and the median activation supersaturation $\widetilde{S}_{\mathrm{act}}$. Both quantities are weighted by multiplicity.

Case	$\bar{\tau}_{\mathrm{act}}$ [s]	$\widetilde{S}_{\mathrm{act}}$ [%]
T13	967	0.29
T53	1084	0.12
T73	1268	0.07

clusters. The bimodality reflects a substantially higher frequency of reactivation events under clean conditions. Trajectory-level counting of r_{crit} crossings yields an average of 0.92 reactivations per trajectory in T13, compared with 0.57 in T53 and 0.21 in T73. Because peak supersaturation is progressively suppressed with aerosol loading, deactivated particles in T53 and T73 rarely re-cross r_{crit}, whereas sustained supersaturation in T13 (Fig. 3a) continues to supply conditions above the critical threshold after earlier subcritical excursions. The early mode of the T13 PDF therefore includes both first-time activations during the initial updraft and later reactivations of previously deactivated particles. Cluster-wise CDFs diverge at early times, indicating that activation timing is strongly conditioned by the humidity history specific to each regime. The distributions become more unimodal in T53 and the cluster-wise CDFs collapse toward a common trajectory, indicating reduced inter-cluster disparity. Under the highest aerosol loading (T73), activation is not only delayed but also more synchronized across clusters. Cluster-wise central tendencies converge, although the tails of the activation-time distribution broaden with increasing dilution. The shell cluster activates over a narrow, concentrated window once the supersaturation threshold is exceeded, while core and transition clusters retain broader tails at early and late times that are tied to localized dynamical variability. This compressed activation pattern is consistent with the reduced inter-cluster spread in the RH and radius histories shown for the polluted case in Fig. S4.

Further, the identified relationship between the more synchronized, compressed activation and the reduced inter-cluster spread in T73 points to a strong aerosol control on the supersaturation budget. Stronger competition for water vapor constrains peak supersaturation and shortens the interval of positive supersaturation. Activation then becomes controlled more by the timing of cloud-scale updraft pulses than by modest differences among clusters, which reduces cluster sensitivity in T73. This behavior aligns with parcel-model and turbulent-growth analyses that emphasize rapid supersaturation depletion when droplet number is large (Twomey, 1959; Grabowski and Wang, 2013; Pinsky et al., 2013).

Because the aerosol size-distribution shape is held fixed across T13, T53, and T73, the polluted-case delay should not be interpreted as the appearance of a new coarse-aerosol population. All experiments contain the same dry-size tail. What differs is its activation fate (Oh et al., 2023). In T13, sustained supersaturation allows more of that tail to cross r_{crit} and enter the activated cloud-droplet population. In T53 and T73, more particles remain near or below r_{crit}, and those that do activate have less time to grow by $t = 1400\,\mathrm{s}$ (Fig. 4b). Using the case-mean activation times as a guide, the mean time available for growth after activation is about $430\,\mathrm{s}$ in T13, $320\,\mathrm{s}$ in T53, and only $130\,\mathrm{s}$ in T73. Earlier and less synchronized activation in T13 leaves some droplets much older by that stage, so they can reach collector sizes while many others remain in the cloud-droplet mode. In T73, activation is delayed and compressed into a narrower time window. Therefore, the activated population is younger and

https://doi.org/10.5194/egusphere-2026-3827
Preprint. Discussion started: 21 July 2026

more uniform in size, which limits spectral broadening (Khain et al., 2004; Grabowski and Wang, 2009). In polluted clusters, many activated droplets cannot reach collector size because growth after activation remains weak (Grabowski and Wang, 2013; Hoffmann et al., 2017). The present results show that the aerosol effect is established before collision–coalescence becomes efficient. The suppressed rapid-growth tail in polluted air thus reflects both delayed activation and weak condensational growth after activation.

3.3.5 Cluster-resolved evaluation of the ARG2000 activation closure

Because many climate and cloud-resolving models rely on equilibrium-based activation closures such as ARG2000 (Abdul-Razzak and Ghan, 2000), the regime-dependent activation behavior documented above raises the question of whether such closures capture the same aerosol sensitivity. If the finite-time nature of activation matters, the largest closure biases should appear where supersaturation is intermittent and growth time is limited. This test is most informative in the polluted cases, where activation is delayed and more synchronized (Fig. 5). To evaluate it, the activated droplet number predicted by ARG2000 is diagnosed under the corresponding thermodynamic conditions and compared to the Lagrangian activation diagnosis, stratified by regimes identified from RH history (Fig. 6). In the clean case, agreement is good across all clusters and for the domain-wide total. A progressively larger relative overprediction by ARG2000 emerges in T53 and, most clearly, in T73, visible across all clusters and in the domain total on the logarithmic axis of Fig. 6. Core-like clusters (Clusters 1 and 2) show moderate overprediction because their near-adiabatic conditions are closest to the equilibrium assumptions of the parameterization. The transition cluster (Cluster 3) exhibits a larger bias, and the bias is strongest in entrained-shell conditions (Cluster 4), where intermittent supersaturation departs most from the steady-state framework. The biases, perhaps unsurprisingly, are not uniform offsets. They track intermittent supersaturation exposure and mixing pathways, where a diagnostic peak-supersaturation framework may overestimate how many CCN actually activate within the finite time available. The increasing overprediction with aerosol loading, largest in entrained-shell conditions, shows that peak supersaturation alone is not sufficient for activation. Intermittent supersaturation and limited growth time can prevent CCN from reaching the critical radius even when the peak value exceeds the threshold assumed by the parameterization. This regime dependence motivates treating activation as a finite-time relaxation toward an equilibrium predictor rather than an instantaneous threshold closure (Chuang et al., 1997; Nenes et al., 2001), as discussed further in Sect. 4.

3.4 Lagrangian diagnostics of entrainment-mixing, activation, and deactivation

The analysis based on clusters above separates trajectories by their moisture history but does not directly quantify how entrainment-driven mixing events alter the droplet population as a whole. Therefore, Fig. 7 shows a diagnostic of mixing episodes across the whole population, based on all super-droplets that experience subsaturated exposure and without reference to pre-assigned clusters.

A mixing episode is defined here as a contiguous interval with $\mathrm{RH} < 100\ \%$ for all super-droplets residing in a given grid cell during a temporal bin of $\Delta t = 30\,\mathrm{s}$. Each point in the figure represents one such episode. The survival fraction of activated droplets, $N_{\mathrm{after}}/N_{\mathrm{before}}$, appears on the horizontal axis, and the conditional ratio of droplet volume, $r^3_{\mathrm{v,after}}/r^3_{\mathrm{v,before}}$, appears

https://doi.org/10.5194/egusphere-2026-3827
Preprint. Discussion started: 21 July 2026

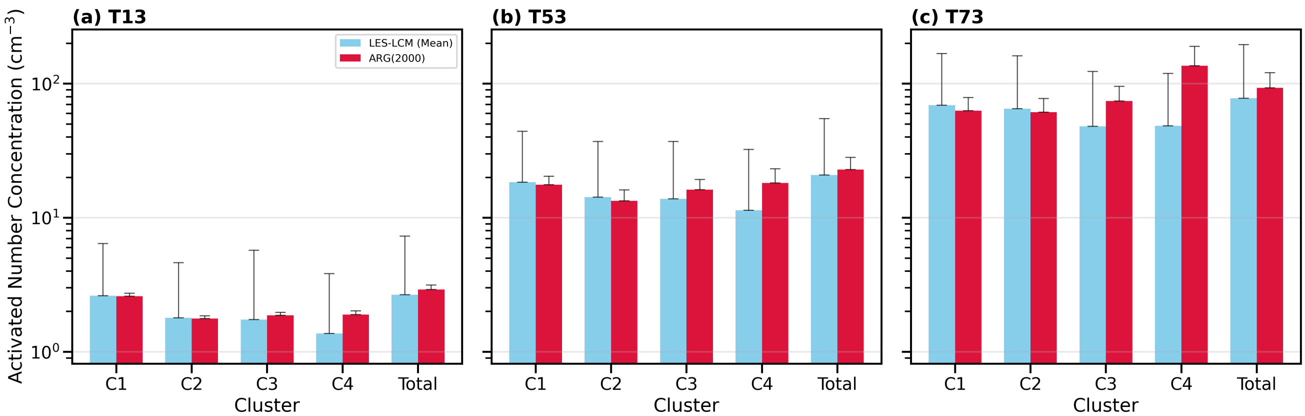

Figure 6. Comparison of activated droplet number concentration for each cluster between the LES–LCM diagnosis (blue) and the Abdul-Razzak and Ghan (2000) parameterization, ARG2000 (red), for T13, T53, and T73. Lagrangian trajectories are classified into four clusters (C1–C4) by k-means clustering on relative humidity (RH) features, with Total denoting the average over the whole domain. Light-blue bars show the LES–LCM mean activated number concentration, computed as the arithmetic mean over occupied native $20\,\mathrm{m}$ grid-cell concentrations diagnosed from the first activated point along trajectories. Red bars show the ARG2000 prediction obtained from repeated single-mode evaluations using the sampled set of trajectory-specific vertical velocities together with cluster-level temperature, pressure, aerosol number concentration, and fitted aerosol size-distribution parameters. Error bars are one-sided and indicate $+1\sigma$. For the LES–LCM, they represent the standard deviation across occupied grid-cell concentrations. For ARG2000, they represent the standard deviation across the repeated predictions obtained from the sampled vertical velocities. The vertical axis is logarithmic and expressed in cm^{-3}.

on the vertical axis, where $r_\mathrm{v} \equiv \left(\frac{3}{4\pi}\overline{V_\mathrm{drop}}\right)^{1/3}$ is the mean volume radius of the activated subset. Columns show the early, mid, and late simulation periods ($600\,\mathrm{s}$ to $1000\,\mathrm{s}$, $1000\,\mathrm{s}$ to $1400\,\mathrm{s}$, and $1400\,\mathrm{s}$ to $1800\,\mathrm{s}$), and rows correspond to T13, T53, and T73. The horizontal reference line marks the inhomogeneous-like benchmark and the vertical line denotes the no-loss limit in homogeneous mixing. Because $r_{\mathrm{v,after}}$ is conditioned on the surviving activated subset, values slightly above unity can occur. Here, "inhomogeneous-like" refers to proximity to the horizontal reference line, where surviving activated droplets shrink little, whereas "deactivation-dominated" refers to episodes in which droplet loss is stronger than shrinkage of the surviving activated subset. The two descriptions are related but not identical. This diagnostic adapts the entrainment–mixing diagram of Burnet and Brenguier (2007) and Lehmann et al. (2009), which plots observed droplet number and volume relative to adiabatic reference values. Here, the reference state is replaced by the episode-start values, and each point represents one mixing episode diagnosed from the LES–LCM output rather than an in situ sample. Warm-cumulus observations likewise show that the apparent mixing signature can vary with height and local turbulence structure (Small et al., 2013). Sensitivity tests confirm that the median coordinates of the mixing diagram are robust to the choice of temporal bin width ($15\,\mathrm{s}$ to $60\,\mathrm{s}$) and vertical bin depth ($25\,\mathrm{m}$ to $100\,\mathrm{m}$), with variations confined to the third decimal place.

https://doi.org/10.5194/egusphere-2026-3827
Preprint. Discussion started: 21 July 2026

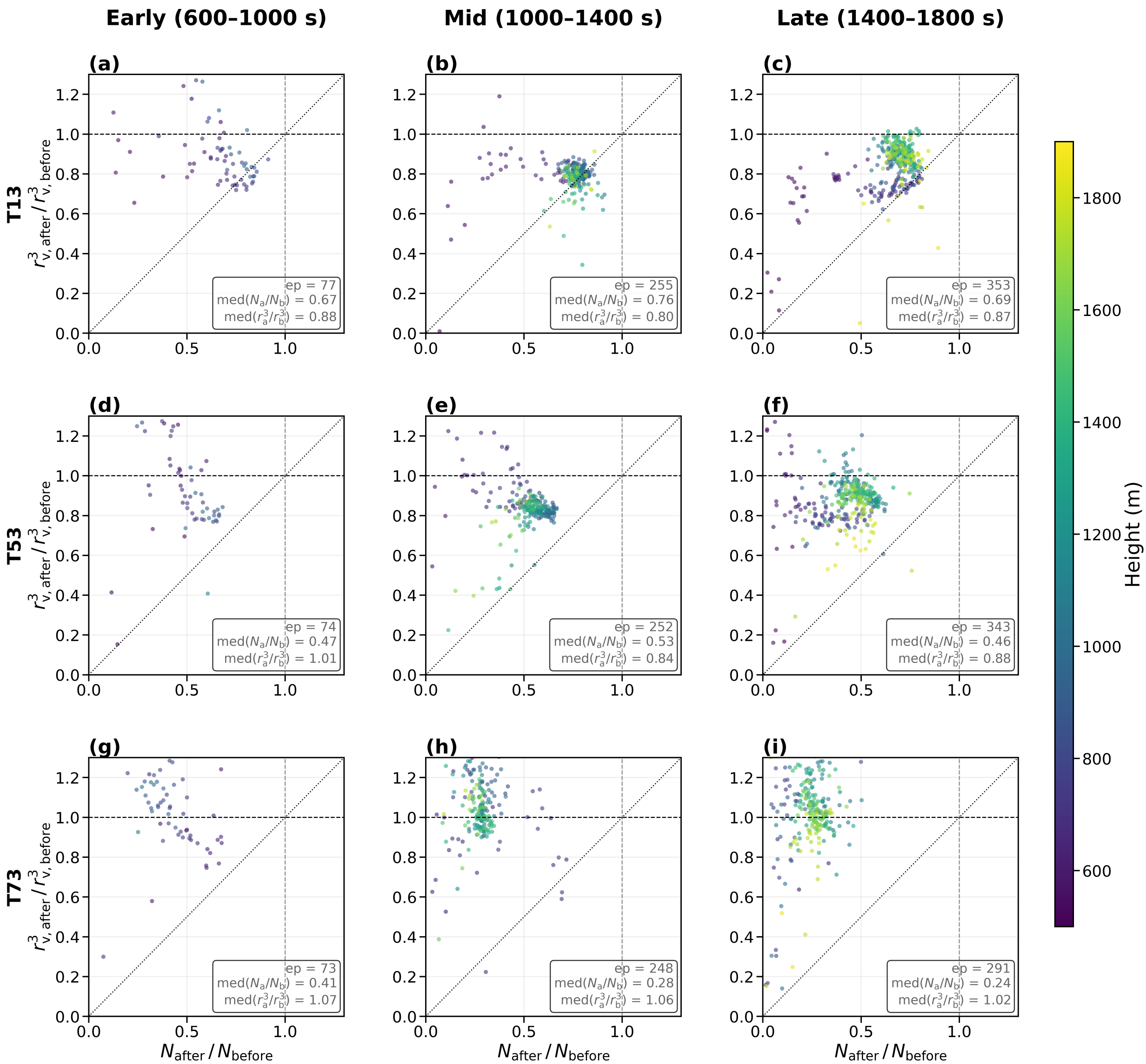

Figure 7. Lagrangian diagrams of mixing events for the whole population in T13 (top), T53 (middle), and T73 (bottom). Columns show the early (600 s to 1000 s), mid (1000 s to 1400 s), and late (1400 s to 1800 s) periods. The horizontal axis shows the survival fraction of activated droplets $N_{\mathrm{after}}/N_{\mathrm{before}}$ and the vertical axis shows the conditional ratio of droplet volume $r^3_{\mathrm{v,after}}/r^3_{\mathrm{v,before}}$. Each point represents one height–time binned mixing episode. Colors indicate the mean height of each episode. The horizontal dashed line marks the inhomogeneous-like reference, the vertical line denotes the no-loss limit, and the diagonal marks equal fractional reduction in droplet number and volume.

https://doi.org/10.5194/egusphere-2026-3827
Preprint. Discussion started: 21 July 2026

Mixing characteristics show a clear aerosol dependence across all periods. In the clean case T13 (Fig. 7a–c), episodes cluster near the diagonal with relatively high survival fractions (median $N_{\mathrm{after}}/N_{\mathrm{before}} = 0.67$–$0.76$) accompanied by reduced mean volume (median $r^3_{\mathrm{v,after}}/r^3_{\mathrm{v,before}} = 0.80$–$0.88$). This pattern points to transitional behavior in which partial evaporation reduces the size of surviving droplets while a smaller fraction deactivates. In T53 (Fig. 7d–f), survival decreases (median 0.46–0.53) while the volume ratio remains closer to unity (median 0.84–1.01), indicating more deactivation-dominated behavior together with a shift toward the inhomogeneous-like reference, with comparatively limited shrinkage of the remaining activated subset. The most polluted case T73 (Fig. 7g–i) exhibits the strongest inhomogeneous-like signature. Episodes concentrate at low survival (median 0.24–0.41) with near-unity or slightly super-unity volume ratios (median 1.02–1.07), pointing to preferential deactivation of the smallest droplets, which increases the conditional mean volume of the remaining activated population. High aerosol loading leaves a droplet population dominated by small radii that remain close to r_{crit}. Evaporation time scales vary with r^2 (Lu et al., 2018), so brief subsaturated excursions preferentially remove small droplets rather than shrinking the survivors. The preferential removal pushes the mixing points toward the inhomogeneous reference, in line with Lagrangian mixing diagnostics reported in particle-based models (Hoffmann et al., 2019; Kainz and Hoffmann, 2023). Suppressed collision–coalescence in T73 limits size separation and keeps more droplets vulnerable to deactivation. The number of episodes increases from the early period ($\sim$73–77) to the late period (291–353), reflecting cloud-field development. The polluted case also shows a systematic temporal shift toward lower survival. In T73, the median falls from 0.41 to 0.28 and then to 0.24. Colors further indicate reduced survival at higher altitudes, particularly in T53 and T73, due to stronger subsaturation associated with cloud-top entrainment. Taken together with the delayed activation (Fig. 5) and the weaker activated upper tail (Fig. 4), the mixing-episode analysis reinforces the picture that higher aerosol loading promotes preferential deactivation of small droplets while leaving the surviving population spectrally narrow, which limits the supply of collector drops needed for precipitation initiation.

The shift toward lower survival and more deactivation-dominated behavior under higher aerosol loading reflects the fact that polluted droplets are smaller and closer to their critical radius, so they deactivate more readily during subsaturated excursions. The emergence of a robust inhomogeneous-like signature in T73 at grid-scale resolution is qualitatively consistent with the findings of Lim and Hoffmann (2024), who used the L3 framework (LES–LCM coupled to a linear eddy model) at sub-meter resolution and reported that inhomogeneous mixing becomes increasingly prevalent as shallow cumulus ages and aerosol loading rises. Lim and Hoffmann (2024) classified mixing scenarios into homogeneous, inhomogeneous, and narrowing categories using the inhomogeneous mixing degree (IHMD) index derived from Lagrangian particle tracking at sub-meter resolution. The present diagnostic instead focuses on how the survival fraction and conditional volume change of the activated subset respond to aerosol loading, using episode-level statistics at grid-scale resolution. The present simulations do not use the L3 framework, so the comparison is qualitative rather than one-to-one.

A recent observational analysis by D'Alessandro et al. (2025), based on in situ measurements from the Aerosol and Cloud Experiments in the Eastern North Atlantic (ACE-ENA) and other field campaigns, points in a similar statistical direction, with inhomogeneous classifications occurring more frequently in higher-aerosol, non-precipitating samples and homogeneous classifications occurring more often in lower-aerosol, lower-droplet-concentration samples. The comparison remains indirect

https://doi.org/10.5194/egusphere-2026-3827
Preprint. Discussion started: 21 July 2026

because the observational classification is based on campaign-scale in situ diagnostics and direct DSD contrasts rather than on the population-based LES metrics used here. Aircraft observations of warm cumulus from the Gulf of Mexico Atmospheric Composition and Climate Study (GoMACCS) point in a similar direction (Small et al., 2013). In those data, inhomogeneous mixing explains much of the liquid-water variability, but the aerosol dependence of mixing type remains suggestive rather than statistically conclusive. This limitation deserves emphasis and supports cautious interpretation of aerosol-sensitive mixing signatures across datasets.

Observationally, similar mixing classifications are inferred from coupled changes in droplet number and droplet size, but the apparent signature depends on sampling scale, height, and local turbulence structure (Small et al., 2013; D'Alessandro et al., 2025). From a Damköhler-number perspective, the polluted cases match a regime in which droplet evaporation and deactivation outpace turbulent homogenization (Lehmann et al., 2009; Kumar et al., 2012). This comparison should be read qualitatively, because the present simulations resolve mixing only at the LES grid scale and do not include a sub-grid representation of turbulent homogenization such as the L3 framework (Hoffmann et al., 2019). Under such conditions, the smallest activated droplets are preferentially removed, while the surviving activated subset undergoes only limited shrinkage, as reported in particle-based mixing diagnostics (Hoffmann et al., 2019; Kainz and Hoffmann, 2023).

3.5 Radar forward modeling of LES–LCM output

The microphysical and mixing diagnostics presented so far rely on quantities that are accessible only within the simulation. To assess whether the aerosol-induced differences identified above remain visible in radar observables, the analysis now turns to radar forward modeling. A Ka-band forward operator applied directly to the particle population at $35\,\mathrm{GHz}$ with exact Mie scattering (Sect. 2.4) translates the super-droplet population into the attenuated equivalent radar reflectivity factor Z_e, mean Doppler velocity V_D, and full Doppler spectra. Three levels of analysis are performed. Time–height fields of Z_e averaged over the domain reveal the large-scale aerosol signature in column structure (Fig. 8). A spectral decomposition into cloud and drizzle components then isolates the contribution from the precipitation mode. Doppler spectra for individual grid cells and the corresponding moment statistics (Fig. 9, Table 5) provide the spectral detail needed to connect microphysical pathway differences to observationally testable quantities.

3.5.1 Domain-averaged reflectivity

Reflectivity structures are strongly aerosol dependent (Fig. 8). T13 develops deeper, more vertically coherent regions of enhanced Z_e, reflecting frequent formation and vertical transport of the large drops that dominate radar backscatter. T73 is systematically weaker and more diffuse, with little contribution from the precipitation mode. T53 falls in between, its enhancement intermittent and patchy.

Because the forward operator is a central methodological component rather than a secondary post-processing step, the radar diagnostics below are interpreted directly through the framework introduced in Sect. 2.4. The preceding sections identified how aerosol loading shifts activation timing, growth after activation, and the precipitation-mode tail in particle space. The forward operator tests whether those same pathway differences remain visible once mapped into quantities that a radar would observe.

https://doi.org/10.5194/egusphere-2026-3827
Preprint. Discussion started: 21 July 2026

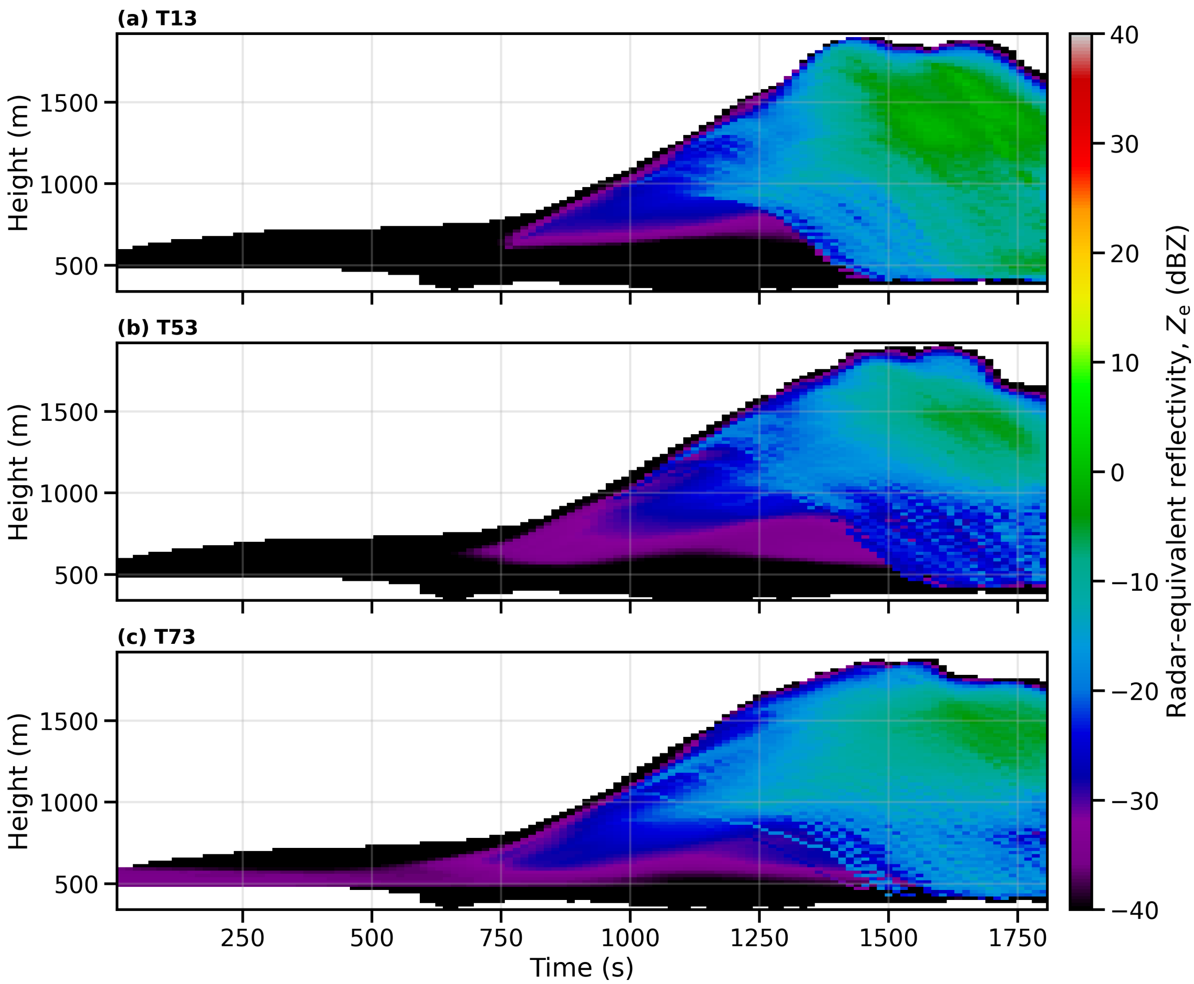

Figure 8. Time–height plots of the Ka-band attenuated equivalent radar reflectivity factor averaged over the domain (Z_e in dBZ) for (a) T13 (top), (b) T53 (middle), and (c) T73 (bottom). Simulation time is shown on the horizontal axis and height on the vertical axis. The clean case develops stronger and more persistent high-reflectivity structures, while the polluted case remains weaker and more diffuse.

https://doi.org/10.5194/egusphere-2026-3827
Preprint. Discussion started: 21 July 2026

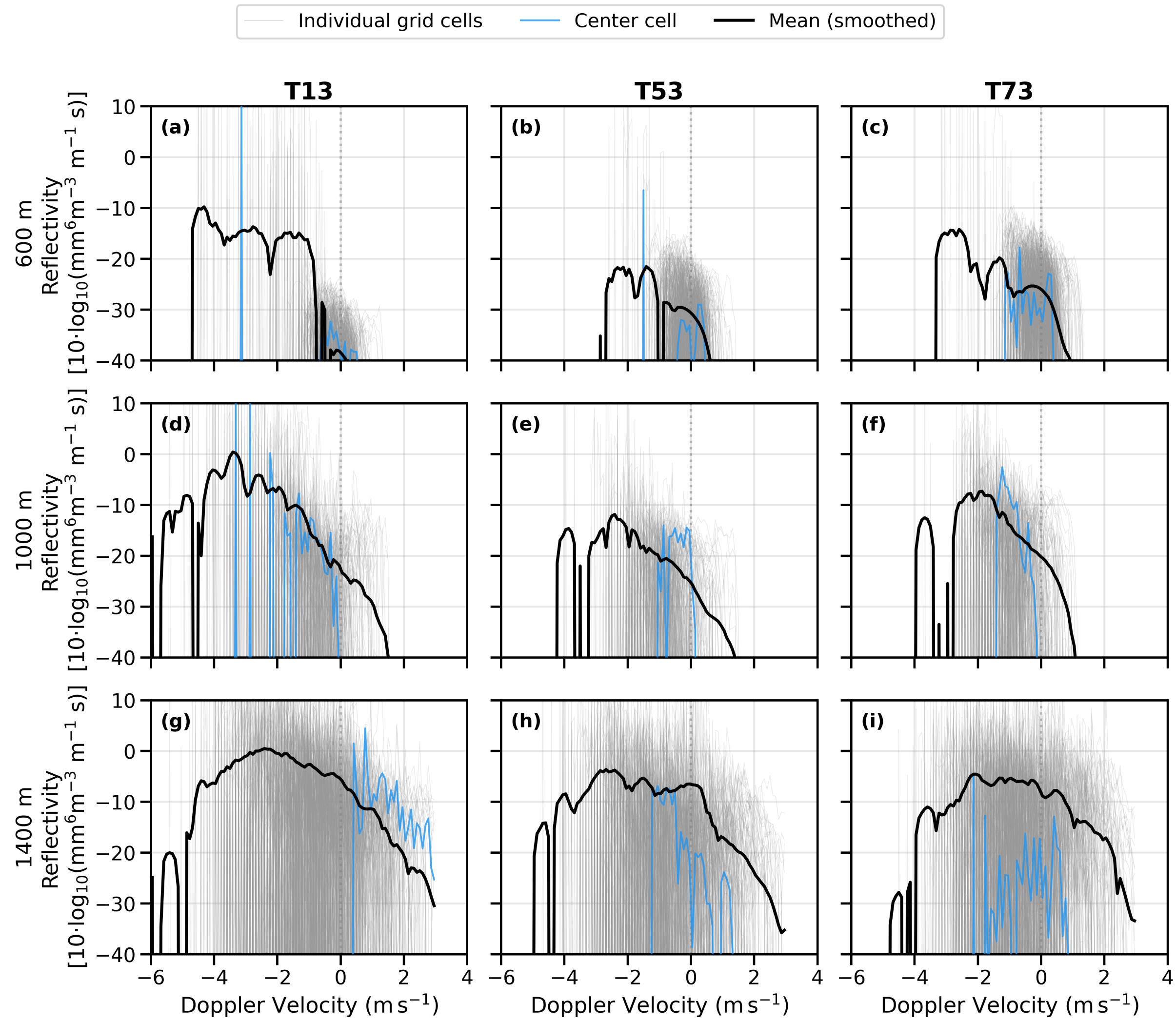

Figure 9. Ka-band (35 GHz) attenuated Doppler spectra for individual grid cells at $t = 1600\,\mathrm{s}$. Columns correspond to T13, T53, and T73. Rows correspond to $z = 600\,\mathrm{m}$, $1000\,\mathrm{m}$, and $1400\,\mathrm{m}$. Doppler velocity ($\mathrm{m\,s^{-1}}$) is shown on the horizontal axis. The vertical axis gives $10\log_{10}[S_{\mathrm{att}}(v)/(1\ \mathrm{mm^6\,m^{-3}}\,(\mathrm{m\,s^{-1}})^{-1})]$, where $S_{\mathrm{att}}(v)$ is the attenuated Doppler spectral reflectivity density. Thin gray curves show individual $60\,\mathrm{m}$ by $60\,\mathrm{m}$ horizontal columns, each formed by aggregating 3×3 native $20\,\mathrm{m}$ grid cells within a $\pm 10\,\mathrm{m}$ height band about the target level. The blue curve shows the spectrum from the column at the domain center ($x = 960\,\mathrm{m}$ to $1020\,\mathrm{m}$, $y = 1920\,\mathrm{m}$ to $1980\,\mathrm{m}$). The thick black curve shows the spectrum averaged over the domain. It is smoothed in linear space using a Savitzky–Golay filter and converted to logarithmic units for display only. The vertical gray dotted line marks $v = 0\ \mathrm{m\,s^{-1}}$. More negative velocities correspond to faster-falling hydrometeors. A more pronounced shoulder at more negative velocities indicates a stronger contribution from the drizzle or rain mode.

https://doi.org/10.5194/egusphere-2026-3827
Preprint. Discussion started: 21 July 2026

Table 5. Doppler-moment statistics averaged over the domain and derived from the Ka-band spectra of individual grid cells in Fig. 9. Z_e is the attenuated equivalent radar reflectivity factor (dBZ), V_D is the mean Doppler velocity weighted by reflectivity ($\mathrm{m\,s^{-1}}$), W is the spectrum width ($\mathrm{m\,s^{-1}}$), and γ is the skewness of the Doppler spectrum. Negative V_D indicates net downward motion.

Case / Height	Z_e [dBZ]	V_D [$\mathrm{m\,s^{-1}}$]	W [$\mathrm{m\,s^{-1}}$]	γ
T13 / 600 m	−8.47	−3.218	1.151	0.485
T13 / 1000 m	0.87	−3.252	0.935	0.343
T13 / 1400 m	4.61	−2.088	1.226	0.384
T53 / 600 m	−20.28	−1.659	0.714	0.846
T53 / 1000 m	−10.66	−2.397	0.989	0.261
T53 / 1400 m	0.29	−1.845	1.329	0.245
T73 / 600 m	−13.75	−2.366	0.836	1.454
T73 / 1000 m	−5.88	−1.970	0.806	−0.086
T73 / 1400 m	−0.40	−1.143	1.232	0.143

The radar analysis is therefore used here as an observational extension of the central aerosol–warm-rain problem rather than as a separate topic.

3.5.2 Decomposition into cloud and drizzle components

Fig. S5 shows the corresponding time–height mean Doppler velocity V_D. In T13, more negative V_D values persist through the mid-cloud layer, reflecting the larger fall speeds of drizzle-sized drops when the averaging is weighted by reflectivity. T73 produces systematically smaller $|V_\mathrm{D}|$ because the suppressed large-drop tail reduces that fall speed once reflectivity weighting is applied. Because both Z_e and V_D combine microphysical and dynamical contributions, a spectral decomposition into cloud and drizzle modes of the simulated particle population is needed to separate them.

Radar moments of low order mix microphysical and dynamical effects, so a decomposition based on the model into cloud ($r < 40\,\mathrm{\mu m}$) and drizzle/rain ($r \geq 40\,\mathrm{\mu m}$) components is applied using the threshold introduced in Sect. 2.4. In T13, the drizzle/rain mode makes a pronounced spectral contribution (Fig. 9), broadening the spectrum toward more negative Doppler velocities. T53 retains a detectable shoulder associated with the drizzle mode, but its amplitude is markedly reduced relative to T13, particularly at mid- and upper levels. T73 is dominated by the cloud-droplet mode, and the spectral power associated with the drizzle mode is strongly reduced. The implication is straightforward. Activation delays and reduced early spectral broadening under higher aerosol loading suppress the precipitation-mode tail, and that suppression shows up directly as a weakened

https://doi.org/10.5194/egusphere-2026-3827
Preprint. Discussion started: 21 July 2026

Doppler signature from the drizzle mode at Ka band. The chain from activation timing and mixing regimes through to radar signatures is now complete. Its implications for activation closures and observational constraints are taken up in Sect. 4.

A complementary view that separates the microphysical and dynamical contributions to the simulated spectra is provided in Fig. S6, which shows reflectivity-weighted PDFs of w_{air} together with $-v_{\mathrm{t}}$ distributions for the cloud and drizzle modes at the same heights. The cloud-mode contribution is confined to $|v_{\mathrm{t}}| \lesssim 0.2\,\mathrm{m\,s^{-1}}$. The drizzle-mode contribution populates the negative-velocity tail down to about $-4\,\mathrm{m\,s^{-1}}$. The w_{air} distributions remain comparable across T13, T53, and T73 at each analysis height, with $\langle w_{\mathrm{air}} \rangle$ within $\pm 0.6\,\mathrm{m\,s^{-1}}$ in all panels. The systematic weakening of drizzle-mode spectral power from T13 to T73 therefore reflects suppressed precipitation-mode growth rather than a difference in cloud-scale dynamics.

The decomposition into cloud and drizzle modes confirms that aerosol loading suppresses the drizzle mode, but it does not reveal how much the spectral shape varies across the cloud field or how the standard radar moments compare with observational benchmarks. Doppler spectra for individual grid cells address both questions (Fig. 9). Spectra from individual grid cells cluster tightly near cloud base but diverge markedly aloft, reflecting the intermittent and localized character of collision–coalescence. The spectrum averaged over the domain broadens with height as contributions from the cloud-droplet mode and the precipitation mode evolve. Table 5 summarizes the corresponding Doppler-moment statistics.

Simulated Z_{e} spans approximately -20 to $+4.6$ dBZ, a range consistent with Ka-band observations of drizzle onset and shallow warm-cloud precipitation (Luke and Kollias, 2013; Acquistapace et al., 2017). At all altitudes, T13 yields the largest Z_{e}, driven by more efficient collision–coalescence under lower aerosol loading. Mean Doppler velocity V_{D} at $z = 1400\,\mathrm{m}$ ranges from $-2.1\ \mathrm{m\,s^{-1}}$ in T13 to $-1.1\ \mathrm{m\,s^{-1}}$ in T73, and $|V_{\mathrm{D}}|$ decreases systematically with increasing aerosol loading above $1000\,\mathrm{m}$. The most negative values occur at mid-levels ($V_{\mathrm{D}} \approx -3.3\ \mathrm{m\,s^{-1}}$ for T13 at $1000\,\mathrm{m}$). In Fig. 9, T13 also develops a clearer drizzle mode shoulder and a more negative V_{D} than the polluted cases. That pattern matches the reported spectral evolution once drizzle becomes established and the contribution from large drops increases (Kollias et al., 2011a; Luke and Kollias, 2013). The systematic ordering across aerosol cases is driven by reduced fall speeds when the averaging is weighted by reflectivity, a consequence of suppressed drizzle growth (Kollias et al., 2011b; Luke and Kollias, 2013). Spectrum widths ($W \approx 0.7\,\mathrm{m\,s^{-1}}$ to $1.3\,\mathrm{m\,s^{-1}}$) exceed those typically reported for non-precipitating stratocumulus yet remain consistent with active drizzle formation in shallow cumulus (Acquistapace et al., 2017). Attenuation primarily rescales spectral power and therefore reduces reflectivity magnitude, while V_{D}, W, and γ remain largely unchanged. The broadening is most pronounced at $z = 1400\,\mathrm{m}$, where both within-column microphysical variability and averaging across columns contribute.

Skewness γ offers a compact indicator of spectral mode structure. In the polluted cases at cloud base, γ reaches 0.85 (T53) and 1.45 (T73), pointing to a pronounced two-mode mixture in which intermittent precipitation coexists with a substantial contribution from the cloud-droplet mode. T13, by contrast, produces lower skewness (0.34–0.49) because the spectrum shifts toward the precipitation mode and becomes more symmetric. This progression from large positive γ at drizzle onset to near-zero values for well-developed precipitation matches the spectral evolution documented by Kollias et al. (2011a), a point that deserves emphasis when interpreting aerosol signatures. Spectral shape and apparent peak separability are, however, strongly affected by the sampling volume (Vogl et al., 2024), and the diversity among individual grid cells evident in Fig. 9 is important when comparing with single-column radar observations. Here, “single-column” means a single vertical profile sampled by a

https://doi.org/10.5194/egusphere-2026-3827
Preprint. Discussion started: 21 July 2026

ground-based vertically pointing radar. Because the present case is an idealized process study triggered by an x-homogeneous warm perturbation, horizontally aggregated spectral statistics are treated here as more informative than any single sampled model column. Real observations are less controlled and remain more sensitive to which column is sampled. The signatures in the radar moments and in the spectra thus complete the causal sequence traced through the preceding analyses. Delayed activation (Fig. 5), a weaker activated upper tail (Fig. 4), and enhanced inhomogeneous-like deactivation (Fig. 7) collectively reduce the precipitation-mode tail, and that reduction maps directly onto weaker Z_e, less negative V_D, and less spectral power from the drizzle mode at Ka band.

3.5.3 Reflectivity–rain-rate relationships

The Z–R relation, where Z denotes Z_e throughout this analysis, offers an observationally accessible summary of this causal sequence because its fitted coefficients can be compared with published benchmarks (Comstock et al., 2004; van Zanten et al., 2005; Wood, 2005; Snodgrass et al., 2009). A complementary perspective on the same aerosol-dependent contrasts emerges when the simulated fields are condensed into Z–R power-law relations, for which an extensive set of observational benchmarks exists. An observationally testable summary of these aerosol-dependent radar signatures is obtained by diagnosing drizzle-class Z–R relations for grid cells containing drizzle droplets with $r \geq 40$ µm (Fig. 10).

The comparison is indirect because the simulations are idealized and are not matched to a specific observational case. The fitted coefficients depend on the idealized dynamics, on stochastic sampling of the rare large-drop tail, on the super-droplet splitting and breakup assumptions, and on the drizzle subset definition itself, since the present analysis uses $r \geq 40$ µm, whereas some observational studies define drizzle with a lower threshold, for example $r \geq 20$ µm in Wood (2005). The main point is the relative evolution across the cloud life cycle. The fitted Z–R values vary substantially over that life cycle, so no single power-law fit represents every stage equally well. For context, Table 6 compiles published observational relations spanning marine stratocumulus drizzle, marine stratiform boundary-layer drizzle, trade-wind shallow cumulus precipitation, and the Marshall–Palmer benchmark. Fig. 10(b) should therefore be interpreted against this regime envelope rather than against a single target curve.

Despite the idealized setup, the simulated coefficients fall within the range spanned by the abovementioned published relations, indicating that the drizzle populations obtained from forward modeling occupy a physically plausible regime. The main result is that T13 traverses a much larger fraction of that envelope over the cloud life cycle than T53 or T73. T13 evolves toward substantially larger a_ZR and b_ZR, consistent with a more developed drizzle mode and a stronger precipitation-relevant tail. T53 and T73 remain confined to much smaller coefficients, characteristic of weak-drizzle conditions in which the cloud-droplet mode still dominates. The clean case therefore shows the strongest life-cycle sensitivity, whereas the polluted cases remain confined to a much narrower weak-drizzle range. From an observational perspective, the persistently small a_ZR in T73, together with the less negative V_D ($-1.1\ \mathrm{m\,s^{-1}}$ versus $-2.1\ \mathrm{m\,s^{-1}}$ in T13 at $z = 1400\,\mathrm{m}$, Table 5) and weak drizzle-mode spectral power (Fig. 9), would be consistent with the polluted-side pathway identified here. Larger coefficients together with a stronger fast-falling drizzle mode would point toward the cleaner, more collision-active pathway.

https://doi.org/10.5194/egusphere-2026-3827
Preprint. Discussion started: 21 July 2026

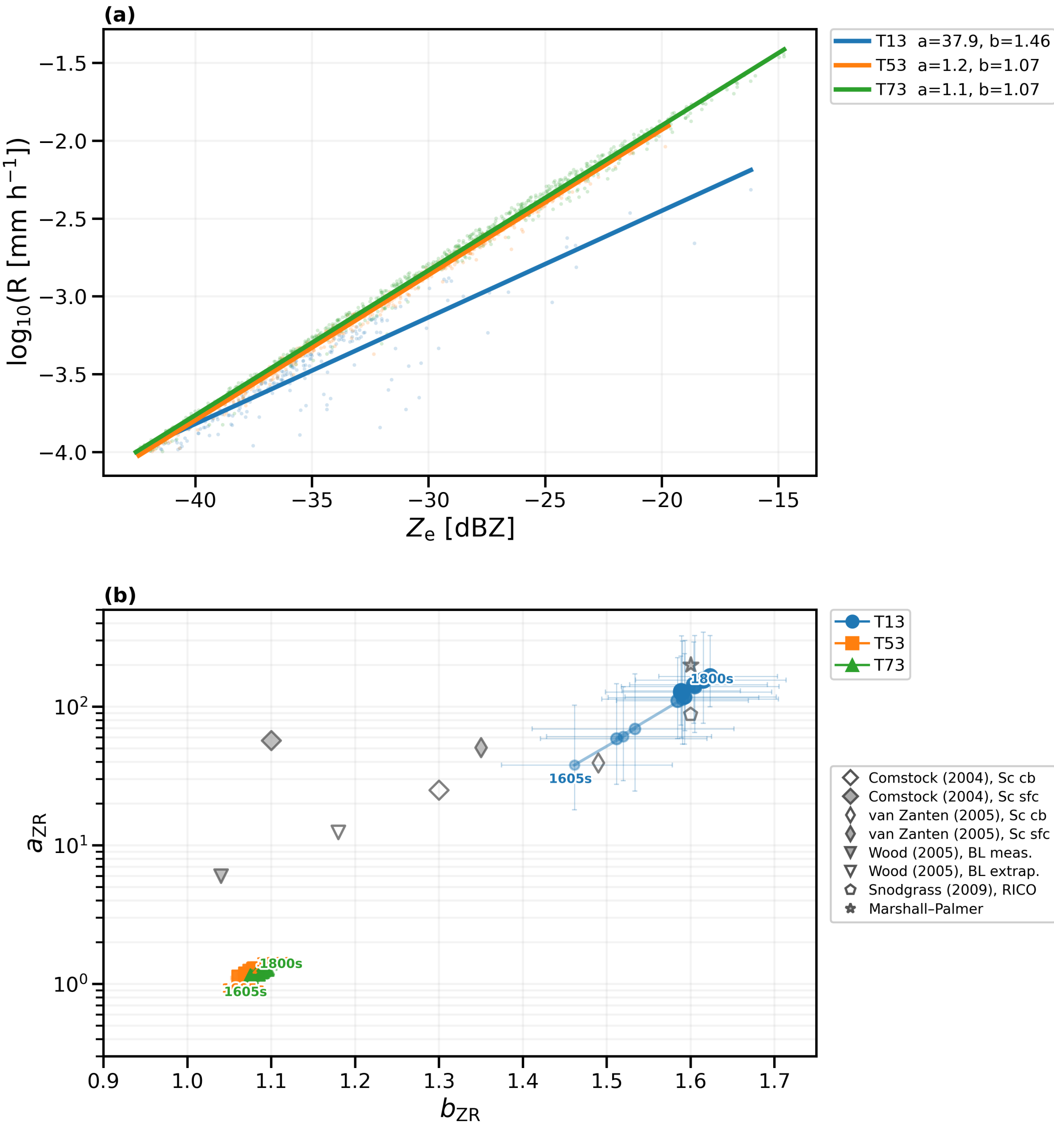

Figure 10. Observationally testable summary of aerosol-dependent drizzle signatures derived from the Ka-band forward simulations. (a) Scatter between attenuated equivalent radar reflectivity factor Z_e and rain rate R for grid cells containing drizzle-class droplets ($r \geq 40$ µm) at $t \approx 1605$ s, shown together with fitted drizzle relations. (b) Temporal evolution of the fitted drizzle-relation parameters a_ZR and b_ZR for the same drizzle-class subset, shown together with selected published observational relations and benchmark curves for context. Colors denote aerosol cases, and labeled markers indicate the early and late analysis times. The comparison is indirect and is intended to aid interpretation of vertically pointing cloud-radar observations rather than to provide case-specific validation. The contextual reference relations shown in panel (b) are summarized in Table 6.

https://doi.org/10.5194/egusphere-2026-3827
Preprint. Discussion started: 21 July 2026

Table 6. Published observational Z–R relations and benchmark curves used for context in Fig. 10(b), based on Marshall and Palmer (1948); Comstock et al. (2004); van Zanten et al. (2005); Wood (2005); Snodgrass et al. (2009). The table documents the contextual curves shown in panel (b). It is not intended as a ranked assessment of transferability across cloud regimes. DYCOMS-II denotes Dynamics and Chemistry of Marine Stratocumulus II, and RICO denotes Rain in Cumulus over the Ocean.

Reference	Regime	a_{ZR}	b_{ZR}	Marker
Comstock et al. (2004), cloud base	Marine stratocumulus drizzle	25	1.30	◇
Comstock et al. (2004), surface	Marine stratocumulus drizzle	57	1.10	◆
van Zanten et al. (2005), DYCOMS-II cloud base	Nocturnal marine stratocumulus drizzle	39.3	1.49	◊
van Zanten et al. (2005), DYCOMS-II surface	Nocturnal marine stratocumulus drizzle	50.9	1.35	⧫
Wood (2005), direct in situ	Marine stratiform boundary-layer drizzle	6.0	1.04	▼
Wood (2005), extrapolated in situ	Marine stratiform boundary-layer drizzle	12.4	1.18	▽
Snodgrass et al. (2009), RICO	Trade-wind shallow cumulus precipitation	88	1.60	○
Marshall–Palmer (1948)	Midlatitude rain benchmark	200	1.60	★

https://doi.org/10.5194/egusphere-2026-3827
Preprint. Discussion started: 21 July 2026

4 Discussion

The most notable feature of the results is that the primary distinction between clean and polluted conditions occurs prior to collision–coalescence becoming efficient. This early imprint has a practical implication. Whenever the aerosol-dependent pathway is set during activation and the growth process through condensation, any approach attempting to measure or parameterize activation as an instantaneous threshold will be unable to distinguish the time-dependent competition shown through trajectory analysis. Models involving parcels or LES–LCM simulations lead to the same mechanism (Twomey, 1959; Grabowski and Wang, 2013; Pinsky et al., 2013; Hoffmann et al., 2017), but a trajectory-level perspective through persistent super-droplet tracking supports the capability to identify the timing of the competition, the regime in which it occurs, and the spatial context. The new HDF5 output structure, which retains both super-droplet information and environmental characteristics, allows for the tracking of approximately 10^8 to 10^9 super-droplets over time.

It is unclear whether the aerosol-dependent pathway seen at the particle level is still apparent after projecting microphysical information onto quantities detectable by a ground-based radar. Previous LES–LCM studies by Hoffmann et al. (2017, 2019), Oh et al. (2023), and Lim and Hoffmann (2024) mainly focused on rain formation through activation pathways and mixing without examining whether the same pathways persist after projection. The results from the forward modeling applied here suggest that the aerosol-dependent pathway differences are still apparent after projection, a point discussed further in the following paragraphs.

The current relationship between warm drizzle and its various Z–R coefficients has been determined through observational studies (Comstock et al., 2004; van Zanten et al., 2005; Wood, 2005; Snodgrass et al., 2009). These coefficients do not provide any insight into how they evolve over the cloud life cycle. The present study therefore tracks the evolution of the Z–R coefficients a_{ZR} and b_{ZR} during a single cloud life cycle experiencing varying amounts of aerosol perturbation. The results indicate that the extent of the temporal range for a_{ZR} and b_{ZR} is also dependent on aerosol content. This may contribute an additional observation-based constraint beyond the typical single-fit approach.

Comparison with observations remains challenging, however, because it depends on sampling volume, temporal averaging, and the exact location of the sampled column (Kollias et al., 2011a; Mech et al., 2020; Vogl et al., 2024). Spectral peak separation depends strongly on sampling volume (Vogl et al., 2024), which limits direct comparison between the idealized setup and any single observed case. Even so, the contrast between aerosol loadings remains clear. When activation is delayed, droplets have less time to grow into the collector-drop range before they deactivate during mixing. The Doppler spectrum then shifts toward weaker drizzle-mode signatures, which may be tested against observed spectra through forward modeling.

The comparison with ARG2000 was intended to quantify how much the explicitly diagnosed activated droplet number in LES–LCM differs from the values predicted by parameterizations used in many present-day climate models. LES–LCM simulation results were therefore compared with the ARG2000 parameterization, which is widely used in global climate models (GCMs) such as the Community Earth System Model / Community Atmosphere Model version 5 (CESM/CAM5) and the UK Met Office Unified Model (Gantt et al., 2014; Ghosh et al., 2025). ARG2000 was selected not because it is the most universally

https://doi.org/10.5194/egusphere-2026-3827
Preprint. Discussion started: 21 July 2026

accurate activation method, but because it is physically based, computationally efficient, widely used in GCMs, and transparent in its assumptions.

The cluster-resolved ARG2000 evaluation (Fig. 6) supports prior findings that activated droplet number alone does not guarantee the formation of a large-drop tail (Grabowski and Wang, 2013; Hoffmann et al., 2017; Oh et al., 2023). The core-like clusters, such as Clusters 1 and 2, differ from the entrained-shell cluster (Cluster 4) not only in peak supersaturation but also in the duration of favorable conditions. ARG2000 performs reasonably well in the core-like clusters because the near-adiabatic assumption is least restrictive there. In the entrained-shell cluster, supersaturation does not persist for long enough, and ARG2000 therefore significantly overpredicts droplet activation. As a result, many super-droplets remain below the critical radius, or only approach it closely, and thus stay on or near the subcritical haze branch. This difference matters because, in the polluted cases, collector-drop formation begins later and leaves less time for diffusional growth. While this analysis shows where and how ARG2000 breaks down, it does not offer an improved activation parameterization as a replacement. Any potential improvement would need to represent not only the maximum supersaturation but also the duration of favorable exposure, the frequency of entrainment interruptions, and the ease with which small droplets deactivate. Alternative activation frameworks support this interpretation. Building on the kinetic-growth limitations identified by Nenes et al. (2001), the population-splitting formulation of Nenes and Seinfeld (2003), later extended by Fountoukis and Nenes (2005), accounts for particles near the activation threshold that do not have enough time to grow efficiently. Exceeding the peak supersaturation therefore does not by itself guarantee activation in that framework. A complementary line of work derives analytical or quasi-steady solutions of the supersaturation budget and links activation time, maximum supersaturation, and activated droplet number directly to the phase-relaxation timescale τ_{phase} and the updraft forcing (Korolev and Mazin, 2003; Khvorostyanov and Curry, 2008). These frameworks do not remove the need for trajectory-resolved analysis in turbulent shallow cumulus. They do, however, support the interpretation that the ARG2000 bias identified here arises because activation is time-limited and intermittently interrupted by mixing rather than controlled by an instantaneous threshold alone.

The mixing diagram provides a useful diagnostic, but its homogeneous and inhomogeneous reference lines do not mark strict physical boundaries and instead serve as guides for organizing the droplet response. The same caution applies to the RH-history-based clusters. They represent different thermodynamic pathways rather than sharply defined dynamical categories with well-defined boundaries. The same fixed value, $k = 4$, is applied to T13, T53, and T73 to preserve a common regime definition across cases. That choice aids inter-case comparison. It may, however, mask case-dependent differences in the number of physically distinct humidity pathways. Weighting by mass or reflectivity would emphasize the larger droplets. Aircraft data confirm this pattern and demonstrate that apparent mixing type shifts with sampling scale, altitude, and local turbulence structure (Small et al., 2013; D'Alessandro et al., 2025). Further analysis using the Damköhler number would strengthen this interpretation, since it would connect the diagnosed mixing signatures more directly to the competition between turbulent homogenization and droplet evaporation, neither of which was quantified in the current study.

The setup is deliberately idealized. Both large-scale forcing and aerosol loading were uniformly scaled by number at fixed size-distribution shape. The specific values obtained would very likely change with a fully forced cloud field or a different aerosol perturbation. The link between delayed activation and weaker drizzle-mode radar signatures, however, may be more

https://doi.org/10.5194/egusphere-2026-3827
Preprint. Discussion started: 21 July 2026

robust than the exact numbers. LES–LCM studies that explicitly represent mixing heterogeneity also report stronger inhomogeneous behavior with increasing aerosol loading (Hoffmann et al., 2019; Lim and Hoffmann, 2024). The present analysis complements those findings by demonstrating how the polluted-side tendency toward delayed activation translates into weaker drizzle-mode radar signatures. The magnitude of this effect in a broader cloud population remains uncertain.

5 Summary and conclusions

The impact of aerosol perturbations on shallow cumulus cloud development occurs primarily via microphysical processes which start with aerosol activation and continue through diffusional growth until collision–coalescence occurs. To trace this progression, we used a BOMEX-based shallow-cumulus case and performed a series of experiments using large-eddy simulations coupled to a Lagrangian cloud microphysics model (LES–LCM). During the experiments, we tested three different aerosol number concentrations (T13, T53, T73): $100\,\mathrm{cm}^{-3}$, $1000\,\mathrm{cm}^{-3}$, and $5000\,\mathrm{cm}^{-3}$. While the shape of the aerosol size-distribution was kept the same across the simulations, the only variable was the number concentration of aerosols. We reconstructed the activation and growth histories of the super-droplets using persistent identifiers, and all statistics were weighted by multiplicity. RH-based clustering separated core-like and entrained-shell-like pathways. A Ka-band radar forward operator was used to derive the attenuated equivalent radar reflectivity factor Z_e, mean Doppler velocity V_D, and Doppler spectra. The average activation time increased from $967\,\mathrm{s}$ (T13) to $1084\,\mathrm{s}$ (T53) and $1268\,\mathrm{s}$ (T73). This indicates that as the concentration of aerosols increased, activation occurred later and in a narrower window of time. The median supersaturation at the time of activation decreased from 0.29 % (T13) to 0.12 % (T53) and 0.07 % (T73). The fact that activation took place later also means that as the time between activation and the onset of collision–coalescence decreased, less time was available for diffusional growth, spectral broadening, and collision–coalescence. Therefore, aerosol effects on the development of short-lived shallow cumulus clouds are established at the early stages of the cloud life cycle. The fraction of trajectories reaching drizzle-relevant sizes ($r \geq 40\,\mathrm{\mu m}$) decreased from 20.1 % in T13 to 15.3 % in T53 and 15.0 % in T73. This reduction reflects both later activation and weaker post-activation growth.

This aerosol-driven contrast in post-activation growth and drizzle formation between the clean and polluted cases was most pronounced along entrained-shell-like pathways, where humidity conditions were least favorable for continued growth and the large-drop tail remained weakest. As aerosol loading increased, mixing episodes shifted toward more deactivation-dominated behavior. The fraction of activated droplets that survived decreased, and conditional mean-volume ratios moved closer to unity. The comparison with ARG2000 exhibited similar regime dependence, with increasing activation bias under higher aerosol loading and the largest bias under entrained-shell conditions. A purely diagnostic equilibrium threshold is therefore difficult to justify in this regime, since encountering supersaturation alone does not guarantee droplet activation. Droplets must remain in a supersaturated environment long enough to grow past their critical radius, despite repeated interruptions by entrainment. The same pathway remained visible in radar diagnostics. Polluted cases produced weaker and less intermittent Z_e, less negative mean Doppler velocity aloft when weighted by reflectivity, and a weaker drizzle-mode shoulder at more negative velocities. Spectral skewness followed the same ordering. Near cloud base, skewness was large and positive in T53 and T73 but lower

https://doi.org/10.5194/egusphere-2026-3827
Preprint. Discussion started: 21 July 2026

in T13. This pattern is consistent with delayed activation, weaker early broadening, and stronger deactivation during mixing. Taken together, these results support comparison with vertically pointing cloud-radar observations, especially when Doppler-spectral structure and sampling strategy are matched carefully.

The analysis is based on a deliberately idealized setup. Large-scale forcing was suppressed, and lower-boundary heat and moisture fluxes were prescribed. Aerosol perturbations changed only number concentration, while the size-distribution shape was held fixed. Stochastic collision–coalescence and the rarity of extreme tail events also add some quantitative sensitivity to super-droplet statistics and random realization. The aerosol-dependent pathway identified here should persist beyond this specific configuration, although its magnitude may change once these idealizations are relaxed. Several directions for future work follow from the present analysis. Coupling the Lagrangian cloud model with the L3 framework will confirm whether the polluted-side shift toward deactivation-dominated, inhomogeneous-like behavior continues when supersaturation fluctuations on sub-grid scales are explicitly represented (Hoffmann et al., 2019; Lim and Hoffmann, 2024). Aerosol recycling after droplet evaporation may also be important in highly polluted environments that often experience deactivation (Shima et al., 2009; Schwenkel and Maronga, 2020). A fully forced cloud field with multiple interacting shallow cumuli would provide a more stringent test of whether the radar signatures identified here survive beyond a single thermally triggered cloud (Siebesma et al., 2003; van Zanten et al., 2011). Ensemble simulations could then help separate robust pathway differences from realization-to-realization variability. More complete radar simulators, such as those that add antenna-beam convolution and finite range-gate averaging to reproduce the observational sampling volume and those that include turbulence-induced spectral broadening and radar noise, would also strengthen the observational side of that comparison. Finally, the study holds high potential for future evaluations against real-world observations. Modern satellite-based cloud tracking approaches, such as those of Seelig et al. (2023), Alexandri et al. (2024), Sokolowsky et al. (2024), and Müller et al. (2025), might soon allow clouds to be classified as a function of life cycle state and environmental aerosol load. This would enable one to relate the evolution of real clouds to the simulated ones, yielding potential to derive model-constrained insights on aerosol effects on clouds.

Code availability. The PALM model system 6.0 is publicly available at https://gitlab.palm-model.org under the GNU General Public License v3. The PAMTRA 1.0 radar forward operator is available at https://github.com/igmk/pamtra (Mech et al., 2020).

Data availability. Simulation results are available at https://doi.org/10.5281/zenodo.19372253 (Lee et al., 2026). Analysis scripts used to produce the figures and diagnostics in this study, along with the super-droplet particle data, are available from the corresponding author upon reasonable request.

Author contributions. JL conducted all simulations, analyzed the data, and wrote the manuscript draft. JL and PS contributed initial ideas and designed experiments. PS, TH and YN supervised the work and revised the paper. All authors actively collaborated in the development of the paper and participated in scientific discussions.

https://doi.org/10.5194/egusphere-2026-3827
Preprint. Discussion started: 21 July 2026

Competing interests. The contact author has declared that they have no competing interests.

Acknowledgements. Views and opinions expressed are those of the author(s) only and do not necessarily reflect those of the European Union or the EuroHPC JU. This project has received funding from the European High Performance Computing Joint Undertaking under grant agreement No. 101234027. It is co-funded by the European Commission, the German Federal Ministry of Research, Technology and Space (BMFTR), the Baden-Württemberg Ministry of Science, Research and the Arts, the Bavarian State Ministry of Science and the Arts and the Lower Saxony Ministry of Science and Culture.

Financial support. This research has been supported by the Deutsche Forschungsgemeinschaft (grant no. 408027490) and by the European Commission Horizon Europe project CleanCloud (grant no. 101137639).

https://doi.org/10.5194/egusphere-2026-3827
Preprint. Discussion started: 21 July 2026

References

Abdul-Razzak, H. and Ghan, S. J.: A parameterization of aerosol activation: 2. Multiple aerosol types, Journal of Geophysical Research: Atmospheres, 105, 6837–6844, https://doi.org/10.1029/1999JD901161, 2000.

Acquistapace, C., Kneifel, S., Löhnert, U., Kollias, P., Maahn, M., and Bauer-Pfundstein, M.: Optimizing observations of drizzle onset with millimeter-wavelength radars, Atmospheric Measurement Techniques, 10, 1783–1802, https://doi.org/10.5194/amt-10-1783-2017, 2017.

Albrecht, B. A.: Aerosols, Cloud Microphysics, and Fractional Cloudiness, Science, 245, 1227–1230, https://doi.org/10.1126/science.245.4923.1227, 1989.

Alexandri, F., Müller, F., Choudhury, G., Achtert, P., Seelig, T., and Tesche, M.: A cloud-by-cloud approach for studying aerosol–cloud interaction in satellite observations, Atmospheric Measurement Techniques, 17, 1739–1757, https://doi.org/10.5194/amt-17-1739-2024, 2024.

Arabas, S., Jaruga, A., Pawlowska, H., and Grabowski, W. W.: libcloudph++ 1.0: a single-moment bulk, double-moment bulk, and particle-based warm-rain microphysics library in C++, Geoscientific Model Development, 8, 1677–1707, https://doi.org/10.5194/gmd-8-1677-2015, 2015.

Baker, M. B., Corbin, R. G., and Latham, J.: The influence of entrainment on the evolution of cloud droplet spectra: I. A model of inhomogeneous mixing, Quarterly Journal of the Royal Meteorological Society, 106, 581–598, https://doi.org/10.1002/qj.49710644914, 1980.

Bellouin, N., Quaas, J., Gryspeerdt, E., Kinne, S., Stier, P., Watson-Parris, D., Boucher, O., Carslaw, K. S., Christensen, M., Daniau, A.-L., Dufresne, J.-L., Feingold, G., Fiedler, S., Forster, P., Gettelman, A., Haywood, J. M., Lohmann, U., Malavelle, F., Mauritsen, T., McCoy, D. T., Myhre, G., Müllmenstädt, J., Neubauer, D., Possner, A., Rugenstein, M., Sato, Y., Schulz, M., Schwartz, S. E., Sourdeval, O., Storelvmo, T., Toll, V., Winker, D., and Stevens, B.: Bounding Global Aerosol Radiative Forcing of Climate Change, Reviews of Geophysics, 58, e2019RG000 660, https://doi.org/10.1029/2019RG000660, 2020.

Bohren, C. F. and Huffman, D. R.: Absorption and Scattering of Light by Small Particles, John Wiley & Sons, New York, 1983.

Bony, S., Stevens, B., Ament, F., Bigber, S., Chepfer, H., Christensen, H., Dufresne, J.-L., Emanuel, K., Ewald, F., Fast, J. D., Fiore, A. M., Flamant, C., Gallardo, L., Hammann, E., Hartmann, D. L., Heyn, I., Kölling, T., Mayer, B., Nuijens, L., Rauber, R. M., Roca, R., Rosenfeld, D., Schulz, H., Stevens, D. E., Sullivan, P. P., Wedemeyer, S., Weinzierl, B., Wendisch, M., Wirth, M., and Züger, B.: EUREC^{4}A: A Field Campaign to Elucidate the Couplings Between Clouds, Convection and Circulation, Surveys in Geophysics, 38, 1529–1568, https://doi.org/10.1007/s10712-017-9428-0, 2017.

Boucher, O., Randall, D., Artaxo, P., Bretherton, C., Feingold, G., Forster, P., Kerminen, V.-M., Kondo, Y., Liao, H., Lohmann, U., Rasch, P., Satheesh, S. K., Sherwood, S., Stevens, B., and Zhang, X.-Y.: Clouds and Aerosols, in: Climate Change 2013: The Physical Science Basis. Contribution of Working Group I to the Fifth Assessment Report of the Intergovernmental Panel on Climate Change, pp. 571–657, Cambridge University Press, Cambridge, UK, https://doi.org/10.1017/CBO9781107415324.016, 2013.

Burnet, F. and Brenguier, J.-L.: Observational Study of the Entrainment-Mixing Process in Warm Convective Clouds, Journal of the Atmospheric Sciences, 64, 1995–2011, https://doi.org/10.1175/JAS3928.1, 2007.

Calinski, T. and Harabasz, J.: A dendrite method for cluster analysis, Communications in Statistics, 3, 1–27, https://doi.org/10.1080/03610927408827101, 1974.

Chandrakar, K. K., Morrison, H., Grabowski, W. W., and Bryan, G. H.: Comparison of Lagrangian Super-Droplet and Eulerian Double-Moment Spectral Microphysics Schemes in Large-Eddy Simulations of an Isolated Cumulus-Congestus Cloud, Journal of the Atmospheric Sciences, 79, 1887–1910, https://doi.org/10.1175/JAS-D-21-0138.1, 2022.

https://doi.org/10.5194/egusphere-2026-3827
Preprint. Discussion started: 21 July 2026

Chuang, P. Y., Charlson, R. J., and Seinfeld, J. H.: Kinetic limitations on droplet formation in clouds, Nature, 390, 594–596, https://doi.org/10.1038/37576, 1997.

Comstock, K. K., Wood, R., Yuter, S. E., and Bretherton, C. S.: Reflectivity and rain rate in and below drizzling stratocumulus, Quarterly Journal of the Royal Meteorological Society, 130, 2891–2918, https://doi.org/10.1256/qj.03.187, 2004.

D'Alessandro, J. J., Wood, R., and Blossey, P. N.: Evaluating Entrainment–Mixing Characteristics through Direct Comparisons of Drop Size Distributions Using In Situ Observations from ACE-ENA, Journal of the Atmospheric Sciences, 82, 2521–2540, https://doi.org/10.1175/JAS-D-24-0153.1, 2025.

de Jong, E., Mackay, J. B., Bulenok, O., Jaruga, A., and Arabas, S.: Breakups are complicated: an efficient representation of collisional breakup in the superdroplet method, Geoscientific Model Development, 16, 4193–4211, https://doi.org/10.5194/gmd-16-4193-2023, 2023.

Devenish, B. J., Bartello, P., Brenguier, J.-L., Collins, L. R., Grabowski, W. W., IJzermans, R. H. A., Malinowski, S. P., Reeks, M. W., Vassilicos, J. C., Wang, L.-P., and Warhaft, Z.: Droplet growth in warm turbulent clouds, Quarterly Journal of the Royal Meteorological Society, 138, 1401–1429, https://doi.org/10.1002/qj.1897, 2012.

Dziekan, P. and Pawlowska, H.: Stochastic coalescence in Lagrangian cloud microphysics, Atmospheric Chemistry and Physics, 17, 13 509–13 520, https://doi.org/10.5194/acp-17-13509-2017, 2017.

Dziekan, P. and Zmijewski, P.: University of Warsaw Lagrangian Cloud Model (UWLCM) 2.0: adaptation of a mixed Eulerian–Lagrangian numerical model for heterogeneous computing clusters, Geoscientific Model Development, 15, 4489–4501, https://doi.org/10.5194/gmd-15-4489-2022, 2022.

Dziekan, P., Waruszewski, M., and Pawlowska, H.: University of Warsaw Lagrangian Cloud Model (UWLCM) 1.0: a modern large-eddy simulation tool for warm cloud modeling with Lagrangian microphysics, Geoscientific Model Development, 12, 2587–2606, https://doi.org/10.5194/gmd-12-2587-2019, 2019.

Fan, C., Wang, M., Rosenfeld, D., Zhu, Y., Liu, J., and Chen, B.: Strong Precipitation Suppression by Aerosols in Marine Low Clouds, Geophysical Research Letters, 47, https://doi.org/10.1029/2019gl086207, 2020.

Feingold, G., Eberhard, W. L., Veron, D. E., and Previdi, M.: First measurements of the Twomey indirect effect using ground-based remote sensors, Geophysical Research Letters, 30, 1287, https://doi.org/10.1029/2002GL016633, 2003.

Forster, P., Storelvmo, T., Armour, K., Collins, W., Dufresne, J.-L., Frame, D., Lunt, D. J., Mauritsen, T., Palmer, M. D., Watanabe, M., Wild, M., and Zhang, H.: The Earth's Energy Budget, Climate Feedbacks and Climate Sensitivity, in: Climate Change 2021: The Physical Science Basis. Contribution of Working Group I to the Sixth Assessment Report of the Intergovernmental Panel on Climate Change, pp. 923–1054, Cambridge University Press, Cambridge, UK, https://doi.org/10.1017/9781009157896.009, 2021.

Fountoukis, C. and Nenes, A.: Continued Development of a Cloud Droplet Formation Parameterization for Global Climate Models, Journal of Geophysical Research: Atmospheres, 110, https://doi.org/10.1029/2004JD005591, 2005.

Gantt, B., He, J., Zhang, X., Zhang, Y., and Nenes, A.: Incorporation of advanced aerosol activation treatments into CESM/CAM5: model evaluation and impacts on aerosol indirect effects, Atmospheric Chemistry and Physics, 14, 7485–7497, https://doi.org/10.5194/acp-14-7485-2014, 2014.

Ghosh, P., Evans, K. J., Grosvenor, D. P., Kang, H.-G., Mahajan, S., Xu, M., Zhang, W., and Gordon, H.: Assessing modifications to the Abdul-Razzak and Ghan aerosol activation parameterization (version ARG2000) to improve simulated aerosol–cloud radiative effects in the UK Met Office Unified Model (UM version 13.0), Geoscientific Model Development, 18, 4899–4913, https://doi.org/10.5194/gmd-18-4899-2025, 2025.

https://doi.org/10.5194/egusphere-2026-3827
Preprint. Discussion started: 21 July 2026

Grabowski, W. W.: Comparison of Eulerian Bin and Lagrangian Particle-Based Microphysics in Simulations of Nonprecipitating Cumulus, Journal of the Atmospheric Sciences, 77, 3397–3412, https://doi.org/10.1175/JAS-D-20-0100.1, 2020.

Grabowski, W. W. and Abade, G. C.: Broadening of Cloud Droplet Spectra through Eddy Hopping: Turbulent Adiabatic Parcel Simulations, Journal of the Atmospheric Sciences, 74, 1485–1493, https://doi.org/10.1175/JAS-D-17-0043.1, 2017.

Grabowski, W. W. and Wang, L.-P.: Diffusional and Accretional Growth of Water Drops in a Rising Adiabatic Parcel: Effects of the Turbulent Collision Kernel, Atmospheric Chemistry and Physics, 9, 2335–2353, https://doi.org/10.5194/acp-9-2335-2009, 2009.

Grabowski, W. W. and Wang, L.-P.: Growth of cloud droplets in a turbulent environment, Annual Review of Fluid Mechanics, 45, 293–324, https://doi.org/10.1146/annurev-fluid-011212-140750, 2013.

Grabowski, W. W., Dziekan, P., and Pawlowska, H.: Lagrangian condensation microphysics with Twomey CCN activation, Geoscientific Model Development, 11, 103–120, https://doi.org/10.5194/gmd-11-103-2018, 2018.

Grabowski, W. W., Morrison, H., Shima, S., Abade, G. C., Dziekan, P., and Pawlowska, H.: Modeling of Cloud Microphysics: Can We Do Better?, Bulletin of the American Meteorological Society, 100, 655–672, https://doi.org/10.1175/BAMS-D-18-0005.1, 2019.

Grabowski, W. W., Thomas, L., and Kumar, B.: Impact of Cloud-Base Turbulence on CCN Activation: CCN Distribution, Journal of the Atmospheric Sciences, 79, 2965–2981, https://doi.org/10.1175/JAS-D-22-0075.1, 2022.

Heus, T., Pols, C. F. J., Jonker, H. J. J., Van den Akker, H. E. A., and Lenschow, D. H.: A statistical approach to the life cycle analysis of cumulus clouds selected in a virtual reality environment, Journal of Geophysical Research: Atmospheres, 114, D06 208, https://doi.org/10.1029/2008JD010910, 2009.

Hill, A. A., Lebo, Z. J., Andrejczuk, M., Arabas, S., Dziekan, P., Field, P., Gettelman, A., Hoffmann, F., Pawlowska, H., Onishi, R., and Vié, B.: Toward a Numerical Benchmark for Warm Rain Processes, Journal of the Atmospheric Sciences, 80, 1329–1359, https://doi.org/10.1175/JAS-D-21-0275.1, 2023.

Hoffmann, F. and Feingold, G.: Entrainment and Mixing in Stratocumulus: Effects of a New Explicit Subgrid-Scale Scheme for Large-Eddy Simulations with Particle-Based Microphysics, Journal of the Atmospheric Sciences, 76, 1955–1973, https://doi.org/10.1175/JAS-D-18-0318.1, 2019.

Hoffmann, F., Raasch, S., and Noh, Y.: Entrainment of aerosols and their activation in a shallow cumulus cloud studied with a coupled LCM–LES approach, Atmospheric Research, 156, 43–57, https://doi.org/10.1016/j.atmosres.2014.12.008, 2015.

Hoffmann, F., Noh, Y., and Raasch, S.: The Route to Raindrop Formation in a Shallow Cumulus Cloud Simulated by a Lagrangian Cloud Model, Journal of the Atmospheric Sciences, 74, 2125–2142, https://doi.org/10.1175/JAS-D-16-0220.1, 2017.

Hoffmann, F., Yamaguchi, T., and Feingold, G.: Inhomogeneous mixing in Lagrangian cloud models: Effects on the production of precipitation embryos, Journal of the Atmospheric Sciences, 76, 113–133, https://doi.org/10.1175/JAS-D-18-0087.1, 2019.

ITU-R: Attenuation by atmospheric gases and related effects, Tech. Rep. Recommendation ITU-R P.676-13, International Telecommunication Union, Radiocommunication Sector, https://www.itu.int/rec/R-REC-P.676, 2022.

Jaenicke, R.: Aerosol physics and chemistry, in: Numerical Data and Functional Relationships in Science and Technology, New Series, Group V: Geophysics and Space Research, Volume 4b: Meteorology, edited by Fischer, G., pp. 391–457, Springer, Berlin, Heidelberg, 1988.

Kainz, J. and Hoffmann, F.: The Effects of Aerosol on Small-Scale Cloud-Environment Mixing: Implications for Simulating and Observing Inhomogeneous Mixing, Journal of Geophysical Research: Atmospheres, 128, e2023JD038 509, https://doi.org/10.1029/2023JD038509, 2023.

Khain, A., Pokrovsky, A., Pinsky, M., Seifert, A., and Phillips, V.: Simulation of Effects of Atmospheric Aerosols on Deep Turbulent Convective Clouds Using a Spectral Microphysics Mixed-Phase Cumulus Cloud Model. Part I: Model Description and Possible Applications, Journal of the Atmospheric Sciences, 61, 2963–2982, https://doi.org/10.1175/JAS-3350.1, 2004.

Khairoutdinov, M. and Kogan, Y.: A New Cloud Physics Parameterization in a Large-Eddy Simulation Model of Marine Stratocumulus, Monthly Weather Review, 128, 229–243, https://doi.org/10.1175/1520-0493(2000)128<0229:ANCPPI>2.0.CO;2, 2000.

Khvorostyanov, V. I. and Curry, J. A.: Kinetics of Cloud Drop Formation and Its Parameterization for Cloud and Climate Models, Journal of the Atmospheric Sciences, 65, https://doi.org/10.1175/2008JAS2606.1, 2008.

Kollias, P., Clothiaux, E. E., Miller, M. A., Albrecht, B. A., Stephens, G. L., and Ackerman, T. P.: Millimeter-Wavelength Radars: New Frontier in Atmospheric Cloud and Precipitation Research, Bulletin of the American Meteorological Society, 88, 1608–1624, https://doi.org/10.1175/BAMS-88-10-1608, 2007.

Kollias, P., Remillard, J., Luke, E., and Szyrmer, W.: Cloud Radar Doppler Spectra in Drizzling Stratiform Clouds. Part I: Forward Modeling and Remote Sensing Applications, Journal of Geophysical Research: Atmospheres, 116, D13 202, https://doi.org/10.1029/2010JD015237, 2011a.

Kollias, P., Szyrmer, W., Remillard, J., and Luke, E.: Cloud Radar Doppler Spectra in Drizzling Stratiform Clouds. Part II: Observations and Microphysical Modeling of Drizzle Evolution, Journal of Geophysical Research: Atmospheres, 116, D13 203, https://doi.org/10.1029/2010JD015238, 2011b.

Korolev, A., Isaac, G. A., Strapp, J. W., Cober, S. G., and Barker, H. W.: In Situ Measurements of Liquid Water Content Profiles in Midlatitude Stratiform Clouds, Quarterly Journal of the Royal Meteorological Society, 133, 1693–1699, https://doi.org/10.1002/qj.147, 2007.

Korolev, A. V. and Mazin, I. P.: Supersaturation of Water Vapor in Clouds, Journal of the Atmospheric Sciences, 60, 2957–2974, https://doi.org/10.1175/1520-0469(2003)060<2957:SOWVIC>2.0.CO;2, 2003.

Kumar, B., Schumacher, J., and Shaw, R. A.: Extreme responses of a coupled scalar–particle system during turbulent mixing, New Journal of Physics, 14, 115 020, https://doi.org/10.1088/1367-2630/14/11/115020, 2012.

Köhler, H.: The nucleus in and the growth of hygroscopic droplets, Transactions of the Faraday Society, 32, 1152–1161, https://doi.org/10.1039/TF9363201152, 1936.

Lanotte, A. S., Seminara, A., and Toschi, F.: Cloud droplet growth by condensation in homogeneous isotropic turbulence, Journal of the Atmospheric Sciences, 66, 1685–1697, https://doi.org/10.1175/2008JAS2864.1, 2009.

Lehmann, K., Siebert, H., and Shaw, R. A.: Homogeneous and Inhomogeneous Mixing in Cumulus Clouds: Dependence on Local Turbulence Structure, Journal of the Atmospheric Sciences, 66, 3641–3659, https://doi.org/10.1175/2009JAS3012.1, 2009.

Lim, J.-S. and Hoffmann, F.: Between Broadening and Narrowing: How Mixing Affects the Width of the Droplet Size Distribution, Journal of Geophysical Research: Atmospheres, 128, e2022JD037 900, https://doi.org/10.1029/2022JD037900, 2023.

Lim, J.-S. and Hoffmann, F.: Life Cycle Evolution of Mixing in Shallow Cumulus Clouds, Journal of Geophysical Research: Atmospheres, 129, e2023JD040 393, https://doi.org/10.1029/2023JD040393, 2024.

Lu, C., Liu, Y., Yum, S. S., Zhao, C., McFarquhar, G. M., Li, Z., and Niu, S.: On Which Microphysical Time Scales to Use in Studies of Entrainment–Mixing Mechanisms in Clouds, Journal of Geophysical Research: Atmospheres, 123, 3740–3756, https://doi.org/10.1002/2017JD027898, 2018.

Luke, E. P. and Kollias, P.: Separating Cloud and Drizzle Radar Moments during Precipitation Onset Using Doppler Spectra, Journal of Atmospheric and Oceanic Technology, 30, 1656–1671, https://doi.org/10.1175/JTECH-D-11-00195.1, 2013.

MacQueen, J. B.: Some Methods for Classification and Analysis of Multivariate Observations, in: Proceedings of the Fifth Berkeley Symposium on Mathematical Statistics and Probability, edited by Le Cam, L. M. and Neyman, J., vol. 1, pp. 281–297, University of California Press, Berkeley, CA, 1967.

Maronga, B., Banzhaf, S., Burmeister, C., Esch, T., Forkel, R., Fröhlich, D., Fuka, V., Gehrke, K. F., Geletič, J., Giersch, S., Gronemeier, T., Groß, G., Heldens, W., Hellsten, A., Hoffmann, F., Inagaki, A., Kadasch, E., Kanani-Sühring, F., Ketelsen, K., Khan, B. A., Knigge, C., Knoop, H., Krč, P., Kurppa, M., Maamari, H., Matzarakis, A., Mauder, M., Pallasch, M., Pavlik, D., Pfafferott, J., Resler, J., Rissmann, S., Russo, E., Salim, M., Schrempf, M., Schwenkel, J., Seckmeyer, G., Schubert, S., Sühring, M., von Tils, R., Vollmer, L., Ward, S., Witha, B., Wurps, H., Zeidler, J., and Raasch, S.: Overview of the PALM model system 6.0, Geoscientific Model Development, 13, 1335–1372, https://doi.org/10.5194/gmd-13-1335-2020, 2020.

Marshall, J. S. and Palmer, W. M.: The Distribution of Raindrops with Size, Journal of Meteorology, 5, 165–166, https://doi.org/10.1175/1520-0469(1948)005<0165:TDORWS>2.0.CO;2, 1948.

Matsushima, T., Nishizawa, S., and Shima, S.: Overcoming computational challenges to realize meter- to submeter-scale resolution in cloud simulations using the super-droplet method, Geoscientific Model Development, 16, 6211–6245, https://doi.org/10.5194/gmd-16-6211-2023, 2023.

Mech, M., Maahn, M., Kneifel, S., Ori, D., Orlandi, E., Kollias, P., Schemann, V., and Crewell, S.: PAMTRA 1.0: the Passive and Active Microwave radiative TRAnsfer tool for simulating radiometer and radar measurements of the cloudy atmosphere, Geoscientific Model Development, 13, 4229–4251, https://doi.org/10.5194/gmd-13-4229-2020, 2020.

Morrison, H., van Lier-Walqui, M., Fridlind, A. M., Grabowski, W. W., Harrington, J. Y., Hoose, C., Korolev, A., Kumjian, M. R., Milbrandt, J. A., Pawlowska, H., Posselt, D. J., Prat, O. P., Reimel, K. J., Shima, S.-i., van Diedenhoven, B., and Xue, L.: Confronting the Challenge of Modeling Cloud and Precipitation Microphysics, Journal of Advances in Modeling Earth Systems, 12, e2019MS001 689, https://doi.org/10.1029/2019MS001689, 2020.

Müller, F., Seelig, T., Schulz, H., Villanueva, D., and Tesche, M.: Tracking Individual Clouds to Assess the Fidelity of High-Resolution Modeling, Geophysical Research Letters, 52, e2025GL115 648, https://doi.org/10.1029/2025GL115648, 2025.

Nenes, A. and Seinfeld, J. H.: Parameterization of Cloud Droplet Formation in Global Climate Models, Journal of Geophysical Research: Atmospheres, 108, https://doi.org/10.1029/2002JD002911, 2003.

Nenes, A., Ghan, S., Abdul-Razzak, H., Chuang, P. Y., and Seinfeld, J. H.: Kinetic limitations on cloud droplet formation and impact on cloud albedo, Tellus B: Chemical and Physical Meteorology, 53, 133–149, https://doi.org/10.3402/tellusb.v53i2.16569, 2001.

Oh, D., Noh, Y., and Hoffmann, F.: Paths From Aerosol Particles to Activation and Cloud Droplets in Shallow Cumulus Clouds: The Roles of Entrainment and Supersaturation Fluctuations, Journal of Geophysical Research: Atmospheres, 128, e2022JD038 450, https://doi.org/10.1029/2022JD038450, 2023.

Oue, M., Tatarevic, A., Kollias, P., Wang, D., Yu, K., and Vogelmann, A. M.: The Cloud-resolving model Radar SIMulator (CR-SIM) Version 3.3: description and applications of a virtual observatory, Geoscientific Model Development, 13, 1975–1998, https://doi.org/10.5194/gmd-13-1975-2020, 2020.

Petters, M. D. and Kreidenweis, S. M.: A single parameter representation of hygroscopic growth and cloud condensation nucleus activity, Atmospheric Chemistry and Physics, 7, 1961–1971, https://doi.org/10.5194/acp-7-1961-2007, 2007.

Pinsky, M., Mazin, I. P., Korolev, A., and Khain, A.: Supersaturation and Diffusional Droplet Growth in Liquid Clouds, Journal of the Atmospheric Sciences, 70, 2778–2793, https://doi.org/10.1175/JAS-D-12-077.1, 2013.

Pruppacher, H. R. and Klett, J. D.: Microphysics of Clouds and Precipitation, Springer, Dordrecht, 1997.

https://doi.org/10.5194/egusphere-2026-3827
Preprint. Discussion started: 21 July 2026

Radenz, M., Bühl, J., Seifert, P., Griesche, H., and Engelmann, R.: peakTree: a framework for structure-preserving radar Doppler spectra analysis, Atmospheric Measurement Techniques, 12, 4813–4828, https://doi.org/10.5194/amt-12-4813-2019, 2019.

Rauber, R. M., Stevens, B., Ochs, H. T., Knight, C., Albrecht, B. A., Blyth, A. M., Fairall, C. W., Jensen, J. B., Lasher-Trapp, S. G., Mayol-Bracero, O. L., Vali, G., Anderson, J. R., Baker, B. A., Bandy, A. R., Burnet, E., Brenguier, J.-L., Brewer, W. A., Brown, P. R. A., Chuang, R., Cotton, W. R., Di Girolamo, L., Geerts, B., Gerber, H., Göke, S., Gomes, L., Heikes, B. G., Hudson, J. G., Kollias, P., Lawson, R. R., Krueger, S. K., Lenschow, D. H., Nuijens, L., O'Sullivan, D. W., Rilling, R. A., Rogers, D. C., Siebesma, A. P., Snodgrass, E., Stith, J. L., Thornton, D. C., Tucker, S., Twohy, C. H., and Zuidema, P.: Rain in Shallow Cumulus Over the Ocean: The RICO Campaign, Bulletin of the American Meteorological Society, 88, 1912–1928, https://doi.org/10.1175/BAMS-88-12-1912, 2007.

Rosenfeld, D., Andreae, M. O., Asmi, A., Chin, M., de Leeuw, G., Donovan, D. P., Kahn, R., Kinne, S., Kivekäs, N., Kulmala, M., Lau, W., Schmidt, K. S., Suni, T., Wagner, T., Wild, M., and Quaas, J.: Global observations of aerosol-cloud-precipitation-climate interactions, Reviews of Geophysics, 52, 750–808, https://doi.org/10.1002/2013RG000441, 2014.

Rousseeuw, P. J.: Silhouettes: A graphical aid to the interpretation and validation of cluster analysis, Journal of Computational and Applied Mathematics, 20, 53–65, https://doi.org/10.1016/0377-0427(87)90125-7, 1987.

Schwenkel, J. and Maronga, B.: Towards a Better Representation of Fog Microphysics in Large-Eddy Simulations Based on an Embedded Lagrangian Cloud Model, Atmosphere, 11, 466, https://doi.org/10.3390/atmos11050466, 2020.

Schwenkel, J., Hoffmann, F., and Raasch, S.: Improving collisional growth in Lagrangian cloud models: development and verification of a new splitting algorithm, Geoscientific Model Development, 11, 3929–3944, https://doi.org/10.5194/gmd-11-3929-2018, 2018.

Seelig, T., Müller, F., and Tesche, M.: Do Optically Denser Trade-Wind Cumuli Live Longer?, Geophysical Research Letters, 50, e2023GL103 339, https://doi.org/10.1029/2023GL103339, 2023.

Seifert, A. and Beheng, K. D.: A double-moment parameterization for simulating autoconversion, accretion and selfcollection, Atmospheric Research, 59–60, 265–281, https://doi.org/10.1016/S0169-8095(01)00126-0, 2001.

Seinfeld, J. H. and Pandis, S. N.: Atmospheric Chemistry and Physics: From Air Pollution to Climate Change, John Wiley and Sons, 3 edn., 2016.

Shaw, R. A.: Particle-Turbulence Interactions in Atmospheric Clouds, Annual Review of Fluid Mechanics, 35, 183–227, https://doi.org/10.1146/annurev.fluid.35.101101.161125, 2003.

Shima, S.-i., Kusano, K., Kawano, A., Sugiyama, T., and Kawahara, S.: The super-droplet method for the numerical simulation of clouds and precipitation: a particle-based and probabilistic microphysics model coupled with a non-hydrostatic model, Quarterly Journal of the Royal Meteorological Society, 135, 1307–1320, https://doi.org/10.1002/qj.441, 2009.

Siebesma, A. P. and Cuijpers, J. W. M.: Evaluation of Parametric Assumptions for Shallow Cumulus Convection, Journal of the Atmospheric Sciences, 52, 650–666, https://doi.org/10.1175/1520-0469(1995)052<0650:EOPAFS>2.0.CO;2, 1995.

Siebesma, A. P., Bretherton, C. S., Brown, A., Chlond, A., Cuxart, J., Duynkerke, P. G., Jiang, H., Khairoutdinov, M., Lewellen, D. C., Moeng, C.-H., Sánchez, E., Stevens, B., and Stevens, D. E.: A Large Eddy Simulation Intercomparison Study of Shallow Cumulus Convection, Journal of the Atmospheric Sciences, 60, 1201–1219, https://doi.org/10.1175/1520-0469(2003)60<1201:ALESIS>2.0.CO;2, 2003.

Small, J. D., Chuang, P. Y., and Jonsson, H. H.: Microphysical imprint of entrainment in warm cumulus, Tellus B: Chemical and Physical Meteorology, 65, 19 922, https://doi.org/10.3402/tellusb.v65i0.19922, 2013.

Snodgrass, E. R., Di Girolamo, L., and Rauber, R. M.: Precipitation Characteristics of Trade Wind Clouds during RICO Derived from Radar, Satellite, and Aircraft Measurements, Journal of Applied Meteorology and Climatology, 48, 464–483, https://doi.org/10.1175/2008JAMC1946.1, 2009.

https://doi.org/10.5194/egusphere-2026-3827
Preprint. Discussion started: 21 July 2026

Sokolowsky, G. A., Freeman, S. W., Jones, W. K., Kukulies, J., Senf, F., Marinescu, P. J., Heikenfeld, M., Brunner, K. N., Bruning, E. C., Collis, S. M., Jackson, R. C., Leung, G. R., Pfeifer, N., Raut, B. A., Saleeby, S. M., Stier, P., and van den Heever, S. C.: tobac v1.5: introducing fast 3D tracking, splits and mergers, and other enhancements for identifying and analysing meteorological phenomena, Geoscientific Model Development, 17, 5309–5330, https://doi.org/10.5194/gmd-17-5309-2024, 2024.

Stevens, B. and Feingold, G.: Untangling aerosol effects on clouds and precipitation in a buffered system, Nature, 461, 607–613, https://doi.org/10.1038/nature08281, 2009.

Thorndike, R. L.: Who Belongs in the Family?, Psychometrika, 18, 267–276, https://doi.org/10.1007/BF02289263, 1953.

Twomey, S.: The nuclei of natural cloud formation part II: The supersaturation in natural clouds and the variation of cloud droplet concentration, Geofis. Pura e Appl., 43, 243–249, https://doi.org/10.1007/BF01993560, 1959.

Twomey, S.: The Influence of Pollution on the Shortwave Albedo of Clouds, Journal of the Atmospheric Sciences, 34, 1149–1152, https://doi.org/10.1175/1520-0469(1977)034<1149:TIOPOT>2.0.CO;2, 1977.

Unterstrasser, S., Hoffmann, F., and Lerch, M.: Collisional growth in a particle-based cloud microphysical model: insights from column model simulations using LCM1D (v1.0), Geoscientific Model Development, 13, 5119–5145, https://doi.org/10.5194/gmd-13-5119-2020, 2020.

van Zanten, M. C., Stevens, B., Vali, G., and Lenschow, D. H.: Observations of Drizzle in Nocturnal Marine Stratocumulus, Journal of the Atmospheric Sciences, 62, 88–106, https://doi.org/10.1175/JAS-3355.1, 2005.

van Zanten, M. C., Stevens, B., Nuijens, L., Siebesma, A. P., Ackerman, A. S., Burnet, F., Cheng, A., Couvreux, F., Jiang, H., Khairoutdinov, M., Kogan, Y., Lewellen, D. C., Mechem, D., Nakamura, K., Noda, A., Shipway, B. J., Slawinska, J., Wang, S., and Wyszogrodzki, A.: Controls on precipitation and cloudiness in simulations of trade-wind cumulus as observed during RICO, Journal of Advances in Modeling Earth Systems, 3, M06 001, https://doi.org/10.1029/2011MS000056, 2011.

Vogl, T., Radenz, M., Ramelli, F., Gierens, R., and Kalesse-Los, H.: PEAKO and peakTree: tools for detecting and interpreting peaks in cloud radar Doppler spectra – capabilities and limitations, Atmospheric Measurement Techniques, 17, 6547–6568, https://doi.org/10.5194/amt-17-6547-2024, 2024.

Wood, R.: Drizzle in Stratiform Boundary Layer Clouds. Part II: Microphysical Aspects, Journal of the Atmospheric Sciences, 62, 3034–3050, https://doi.org/10.1175/JAS3530.1, 2005.